

1 **Transport-driven aerosol differences above and below the canopy of** 2 **a mixed deciduous forest**

3 Alexander A.T. Bui¹, Henry W. Wallace^{1, a}, Sarah Kavassalis², Hariprasad D. Alwe³, James H. Flynn⁴,
4 Matt H. Erickson^{4, b}, Sergio Alvarez⁴, Dylan B. Millet³, Allison L. Steiner⁵, Robert J. Griffin^{1, 6}

5 ¹ Department of Civil and Environmental Engineering, Rice University, Houston, TX, 77005, USA

6 ² Department of Chemistry, University of Toronto, Toronto, ON, M5S 3H6, Canada

7 ³ Department of Soil, Water, and Climate, University of Minnesota, St. Paul, MN 55108, USA

8 ⁴ Department of Earth and Atmospheric Sciences, University of Houston, Houston, TX, 77204, USA

9 ⁵ Department of Climate and Space Sciences and Engineering, University of Michigan, Ann Arbor, MI, 48109, USA

10 ⁶ Department of Chemical and Biomolecular Engineering, Rice University, Houston, TX, 77005, USA

11 ^a now at: Washington State Department of Ecology, Lacey, WA, 98503, USA

12 ^b now at: TerraGraphics Environmental Engineering, Pasco, WA, 99301, USA

13 *Correspondence to:* Robert J. Griffin (rob.griffin@rice.edu)

14 **Abstract.** Exchanges of energy and mass between the surrounding air and plant surfaces occur below, within, and above a
15 forest's vegetative canopy. The canopy also can lead to vertical gradients in light, trace gases, oxidant availability, turbulent
16 mixing, and properties and concentrations of organic aerosols (OA). In this study, a high-resolution time-of-flight aerosol
17 mass spectrometer is used to measure non-refractory submicron aerosol composition and concentration above (30m) and
18 below (6m) a forest canopy in a mixed deciduous forest at the Program for Research on Oxidants: Photochemistry,
19 Emissions, and Transport tower in northern Michigan during the summer of 2016. Three OA factors are resolved using
20 positive matrix factorization: more-oxidized oxygenated organic aerosol (MO-OOA), isoprene-epoxydiol-derived organic
21 aerosol (IEPOX-OA), and 91Fac (a factor characterized with a distinct fragment ion at m/z 91) from both the above- and
22 below-canopy inlets. MO-OOA was most strongly associated with long-range transport from more polluted regions to the
23 south, while IEPOX-OA and 91Fac were associated with shorter-range transport and local oxidation chemistry. Overall
24 vertical similarity in aerosol composition, degrees of oxidation, and diurnal profiles between the two inlets was observed
25 throughout the campaign, which implies that rapid in-canopy transport of aerosols is efficient enough to cause relatively
26 consistent vertical distributions of aerosols at this scale. However, four distinct vertical gradient episodes are identified for
27 OA, with vertical concentration differences (above-canopy minus below-canopy concentrations) in total OA of up to 0.8
28 $\mu\text{g}/\text{m}^3$, a value that is 42% of the campaign average OA concentration of 1.9 $\mu\text{g}/\text{m}^3$. The magnitude of these differences
29 correlated with concurrent vertical differences in either sulfate aerosol or ozone. These differences are likely driven by a
30 combination of long-range transport mechanisms, canopy-scale mixing and local chemistry. These results emphasize the
31 importance of including vertical and horizontal transport mechanisms when interpreting trace gas and aerosol data in
32 forested environments.

33

34 1 Introduction

35 Aerosols play a key role in the energy balance of the Earth's climate system by scattering and absorbing incoming solar
36 radiation and by impacting cloud lifetime and reflectivity (IPCC, 2007). These climatic effects depend strongly on the
37 chemical speciation of the aerosol particles. Approximately 20-90% of submicron aerosol mass worldwide on average has
38 been predicted to be organic material (Kanakidou et al., 2005), and this is supported by field studies in a variety of urban,
39 urban downwind, and rural locations across the Northern Hemisphere (Jimenez et al., 2009; Zhang et al., 2007). The bulk of
40 this organic material is thought to be secondary organic aerosol (SOA), which is formed in the atmosphere by the reaction of
41 volatile organic compounds (VOCs) with oxidants such as hydroxyl radical (OH), ozone (O₃), nitrate radical, and chlorine
42 atom, with the resulting products then partitioning to the particle phase.

43 Precursor VOCs that contribute to SOA formation are emitted from both anthropogenic and biogenic sources. Biogenic
44 VOCs (BVOCs) primarily are emitted into the atmosphere from terrestrial vegetation, and on a global scale, emissions of
45 BVOCs exceed those of anthropogenic VOCs (Fehsenfeld et al., 1992; Guenther et al., 2000, 1995). Major SOA precursor
46 BVOCs include isoprene (C₅H₈) and terpenes. To date, more than 5000 terpene compounds have been identified, including
47 monoterpenes (C₁₀), sesquiterpenes (C₁₅), and diterpenes (C₂₀) (Geron et al., 2000). However, factors such as the addition
48 of functional groups (aldehydes, alcohols, carboxylic acids, alkyl nitrate, etc.) and the wide variety of possible reaction
49 pathways rapidly increase the number of relevant atmospheric VOCs beyond what is initially emitted (Goldstein and
50 Galbally, 2007).

51 If other loss processes, including deposition, were not considered, the final atmospheric fate of the carbon associated
52 with BVOCs would be oxidation to carbon dioxide. However, partitioning of oxidation products to the aerosol phase as
53 SOA interrupts this oxidation sequence. Partitioning of VOC oxidation products between the gas and aerosol phases
54 depends on multiple factors such as the phase and concentration of pre-existing primary OA (POA) or SOA, particulate-
55 phase SOA reactions, and the presence of aerosol liquid water (ALW) (Seinfeld and Pandis, 2006). As a result of the large
56 number of precursor VOCs, the highly non-linear oxidation chemistry, and the presence of multiple aerosol phases in the
57 atmosphere, SOA formation is complex and relatively poorly understood (Goldstein and Galbally, 2007).

58 The physical environment strongly impacts these chemical SOA formation processes. For example, in forested areas in
59 which BVOC emissions are prevalent, the exchanges of energy and mass between the forest and the atmosphere are
60 influenced by the forest's vegetation canopy. Absorption of light by a canopy can diminish the amount of radiation that is
61 received below the canopy, influencing photolysis rates of photolabile species (Baldocchi et al., 1995; Brown et al., 2005;
62 Fuentes et al., 2007; Makar et al., 2017; Schulze et al., 2017) and oxidant availability (Fuentes et al., 2007). Loss of BVOC
63 oxidation products to deposition within the canopy also has been found to be an important factor in determining the
64 oxidative capacity of a forested environment (Pugh et al., 2009).

65 Vertical transport, also influenced by the canopy, likewise impacts the concentrations of BVOC and SOA in forested
66 environments. Roughness elements created by the leaves, branches, and stems in a dense vegetative canopy combined with
67 above-canopy wind shear leads to coherent structures (Finnigan, 2000). These turbulent flow structures contribute to the
68 fluxes of heat, energy, and matter in forest canopies (Thomas and Foken, 2007). The physical motion of coherent structures
69 occurs via two main mechanisms: upward "bursts," in which air is ejected upward from the canopy into the atmosphere, and
70 downward "sweeps," in which air is directed downward from the atmosphere into the canopy. Vertically resolved sonic
71 anemometer measurements, which provide temperature and three-dimensional wind velocity components at each vertical
72 measurement location, can be used to derive in-canopy mixing metrics.

73 The relative magnitudes of timescales for turbulent transport and chemical processing govern how trace compounds are
74 distributed within the canopy (Baldocchi et al., 1995; Fuentes et al., 2007; Steiner et al., 2011). A modeling study by Gao et
75 al. (1993) found that in-canopy chemical processing of isoprene occurs on a much longer timescale than turbulent transport,
76 making in-canopy reactions less important compared to the turbulent transport and emission of isoprene in determining its

77 in-canopy concentrations. On the other hand, for compounds with an estimated chemical loss timescale that is roughly
78 equivalent to the timescales of turbulent transport (e.g., O₃-initiated oxidation of the sesquiterpene β -caryophyllene), rapid
79 in-canopy chemical loss could dominate (Stroud et al., 2005). Furthermore, partitioning to the aerosol-phase was inferred as
80 a potential reason for observations of decreased mixing ratios of oxidation products of very reactive BVOCs in a ponderosa
81 pine forest canopy (Holzinger et al., 2005).

82 Several studies have attempted to model vertical profiles of trace gases and aerosols in a forest canopy considering both
83 chemistry and turbulent transport. Bryan et al. (2012) found that forest canopy-atmosphere interactions were highly
84 sensitive to turbulent mixing parameterizations during a field campaign in northern Michigan. Differences in highly reactive
85 BVOCs and BVOC oxidation products have been estimated above and below the canopy in modeling and measurement
86 efforts (Alwe et al., 2019; Ashworth et al., 2015; Holzinger et al., 2005; Schulze et al., 2017; Stroud et al., 2005; Wolfe and
87 Thornton, 2011). Schulze et al. (2017) found that rapid through-canopy transport (minimum in-canopy residence time of 10
88 min) leads to relatively consistent simulated above- and below-canopy SOA composition and concentration.

89 Because in-canopy mixing plays a role in the vertical distribution of trace gases and aerosols in a forest canopy, vertical
90 differences in OA components and other inorganic aerosol species such as sulfate (SO₄) could be caused by the degree of
91 mixing between the above- and below-canopy environments. During the PROPHET-CABINEX 2009 campaign, the degree
92 of atmosphere-canopy coupling between the above-canopy atmosphere and the forest was analyzed by Steiner et al. (2011).
93 In this study, the degree of coupling was calculated using the ratio of the kinematic heat flux above the canopy to the
94 kinematic heat flux in the upper canopy. Opposing kinematic heat flux directions (negative ratios) imply that the below-
95 canopy environment is uncoupled from the atmosphere. In 2009, coupling conditions ranged between strong coupling
96 (greater than zero but less than the threshold value defined by the slope of a regression between the two heat fluxes), weak
97 coupling (greater than the defined threshold value), and uncoupled (negative). Uncoupled conditions occurred most
98 commonly in the early morning hours between 4AM and 8AM local time. This set of hours represents approximately 30%
99 of every day over the whole 2009 study period. This suggests that early morning hours may contribute to more instances of
100 uncoupled canopy-atmosphere conditions but that coupling between the forest canopy and the atmosphere occurs a majority
101 of the time (Steiner et al., 2011).

102 Past field studies, such as those above a tropical forest in Brazil and a temperate forest in California, found that in-
103 canopy SOA formation, deposition, and thermal gradient effects on gas-particle partitioning all influence net OA fluxes
104 (Farmer et al., 2013). In the same study, the authors found that oxygenated OA tended to deposit in the canopy, whereas the
105 forest canopy released less oxygenated OA. The source of OA fluxes between forests and the atmosphere has been
106 associated with vertical turbulent transport between the forest atmosphere and the surface layer directly above the canopy;
107 however, there have been few studies that have provided high temporal resolution measurements of both OA composition
108 throughout a forest canopy and canopy mixing strength. In a mixed forest in Ontario, Canada, Gordon et al. (2011) found
109 that the frequent occurrence of net upward aerosol flux was associated with decoupled canopy conditions where entrainment
110 of particle-free air from above the canopy created a positive flux above the forest. On the other hand, Whitehead et al.
111 (2010) found that the particle number concentration and submicron particle composition in the trunk space (i.e., below-
112 canopy) and above-canopy environments showed minimal variation with height during daytime due to stronger turbulence
113 and mixing conditions. In light of these limited studies, there is a need for additional measurements and data to inform the
114 exchange of aerosols between the forest and the atmosphere.

115 Recent work from the Program for Research on Oxidants and PHotochemistry, Emissions and Transport (PROPHET)
116 during the Atmospheric Measurements of Oxidants in Summer (AMOS) campaign in 2016 has indicated that flux of
117 isoprene and monoterpenes at the canopy-atmosphere boundary represents over half of the net carbon flux, while oxygenated
118 VOCs (OVOCs) constitute a majority of the species with detectable VOC fluxes (192 of the 236 species with identified
119 molecular formulas). The authors report that the observed and modelled net carbon flux during the campaign was upward
120 (canopy emission) during the campaign in 2016 (Millet et al., 2018). Vertical gradients of BVOCs in this mixed forest
121 environment vary greatly depending on canopy vegetation height, primary emission versus secondary production, and
122 diurnal variability (Alwe et al., 2019). Correlation analysis of VOC vertical gradients suggests that formic acid (HCOOH)

123 originates from a secondary photochemical production. During the same campaign, distinct sample-to-sample variability in
124 the molecular-level aerosol composition (73 +/- 8%) was observed despite less variability in elemental composition of the
125 bulk OA, indicating the chemical complexity of functionalized OA at the site (Ditto et al., 2018).

126 Here, measurements using an Aerodyne high-resolution time-of-flight aerosol mass spectrometer (HR-ToF-AMS) are
127 used to characterize ambient aerosol above and below the canopy in a mixed, deciduous forest during the PROPHET-AMOS
128 campaign in 2016, with the aim of evaluating quantitatively potential chemical and physical phenomena leading to observed
129 differences between particulate matter above and below the forest canopy. These measurements provide data for validation
130 of forest canopy-atmosphere exchange models and allow an assessment of turbulent transport in the forest canopy and the
131 resulting impacts on above- and below-canopy SOA composition and concentration. These data also could assist in the
132 determination of whether or not SOA is forming within the forest canopy.

133 2 Methods

134 2.1 Site description

135 Measurements were made during the PROPHET-AMOS 2016 campaign from 1 July – 31 July 2016. The PROPHET
136 site (45.55° N, 84.78° W) is situated in a temperate, mixed deciduous forest in the northern portion of Michigan's Lower
137 Peninsula at the University of Michigan Biological Station (UMBS). The surrounding forest consists of aspens (60.9%),
138 northern hardwoods (16.6%; maple, beech, birch, ash, and hemlocks), upland conifers (13.3%; white and red pines), non-
139 forest cover types (7.6%; bracken ferns/grass/developed/road), and northern red oak (1.6%) (Cooper et al., 2001; Bergen and
140 Dronova, 2007). The forests in this region are currently undergoing succession, where the dominant aspens have matured
141 and are now being replaced by northern hardwoods and pines (Bergen and Dronova, 2007). It is expected that this new
142 forest composition will shift BVOC emissions from an isoprene-dominated environment to one that is more influenced by
143 monoterpenes (Toma and Bertman, 2012). The height of the forest canopy varies, but the mean canopy height is
144 approximately 22.5 meters (VanReken et al., 2015). The site's physical layout and site meteorology have been described
145 elsewhere (Carroll et al., 2001; Cooper et al., 2001). The PROPHET site features a 31-m scaffolding tower, allowing
146 measurements to be made at variable heights within and above the vegetation canopy.

147 Due to the sparse surrounding population, the PROPHET site at UMBS has minimal local anthropogenic influences.
148 The closest major urban centers include Detroit, Michigan (350 km to the southeast, population: 672,795), Milwaukee,
149 Wisconsin (350 km to the southwest, population: 595,047), and Chicago, Illinois (450 km to the southwest, population:
150 2,704,958) (Carroll et al., 2001). The closest nearby towns include Pellston, Michigan (5 km to the west, population: 828),
151 Petoskey, Michigan (30 km to the southwest, population: 5,749), and Cheboygan, Michigan (30 km to the northeast,
152 population: 4,726). Population totals are based on 2016 population estimates for cities and towns in the United States (US)
153 from the US Census Bureau (US Census Bureau, 2018).

154 The mean temperature during the campaign was 20.6 +/- 4.6 °C (mean +/- one standard deviation), which is 3-4°C
155 warmer than the mean temperature during the 2009 PROPHET-CABINEX campaign (16.9 °C) (VanReken et al., 2015).
156 Temperature conditions during this study are consistent with mean summertime temperatures from studies in 2008 and 2010
157 (Toma and Bertman, 2012) and with historical mean temperature data for the month of July from the Pellston Regional
158 Airport (Figure S1 in the Supplemental Information (SI)). The mean relative humidity (RH) during the campaign was 73.8
159 +/- 17.5% , which is similar to conditions during the CABINEX campaign (74.5 +/- 17.5%) (VanReken et al., 2015). Winds
160 recorded at the top of the PROPHET tower originated mostly from the west, southwest, and northwest (as shown in Figure
161 S2 in the SI). The historical average precipitation according to the National Atmospheric Deposition Program (NADP)
162 National Trends Network for the month of July from 1979-2015 for UMBS is 69.0 +/- 37.8 mm. During the PROPHET-
163 AMOS 2016 campaign, the total accumulated precipitation was 79.0 mm, indicating that precipitation at the site during the
164 campaign was within one standard deviation of the historical July average (NADP, 2016).

165 2.2 Instrumentation and sampling

166 A summary of the trace-gas measurements, instrumentation, and meteorological parameters on board the University of
167 Houston/Rice University Mobile Air Quality Laboratory (MAQL) are summarized in Table S1 of the SI. Details and
168 operation of the MAQL have been described previously in the literature (Leong et al., 2017; Wallace et al., 2018). The
169 MAQL was situated approximately 10 meters to the east of the PROPHET tower. A photograph of the MAQL in stationary
170 sampling mode is shown in Figure S3 in the SI. Table S2 in the SI lists the measurements, measurement methods, and
171 sampling heights of other participating institutions at PROPHET-AMOS 2016 during the campaign. Measurements are
172 reported in local time (LT, Eastern Daylight Time (EDT)) during the campaign.

173 2.2.1 Trace gases

174 Below-canopy trace gases including nitric oxide (NO), nitrogen dioxide (NO₂), total reactive nitrogen (NO_y), O₃, carbon
175 monoxide (CO), and sulfur dioxide (SO₂) were measured from a common inlet on the sampling arm of the MAQL. Reported
176 values of nitrogen oxides (NO_x) represent the sum of NO and NO₂, while reported values of NO_y include NO_x and its
177 reservoir species. These measurements were taken at a height of 6 m above ground level.

178 2.2.2 HR-ToF-AMS

179 The HR-ToF-AMS (Aerodyne Research Inc., USA) was used to measure non-refractory submicron particulate matter
180 (NR-PM₁) from the MAQL; measured composition includes OA, SO₄, nitrate (NO₃), ammonium (NH₄), and chloride (Cl).
181 Detailed descriptions of the operation and principles of the HR-ToF-AMS have been provided elsewhere (DeCarlo et al.,
182 2007). In brief, particles are sampled through a 100-micron critical orifice and are focused into a particle beam using an
183 aerodynamic lens. After traversing a vacuum chamber, the particles in the beam impact onto a tungsten vaporizer heated to
184 600°C. The vapors formed are ionized by electron impact ionization at 70 eV. The resulting ions are detected using a high-
185 resolution time-of-flight mass spectrometer. The HR-ToF-AMS was operated in a high mass sensitivity mode, referred to as
186 V-mode. Ionization efficiency (IE) calibrations were performed at the beginning and end of the campaign using
187 monodisperse 300 nanometer NH₄NO₃ particles. Gas-phase interferences were subtracted from the data based on the
188 observed signal when ambient air was sampled through a filter. Filter zeros were run each day at varying times of day.

189 Sampling was performed from the raised 6-m inlet on the common sampling arm of the MAQL (below canopy) and
190 from a 30-m inlet on the PROPHET tower (above canopy). Copper tubing was used for the sampling inlets, and each inlet
191 was fitted with cyclones to remove particles larger than 2.5 microns in diameter. Prior to the HR-ToF-AMS critical orifice,
192 air was sampled through a nafion dryer to dry the sample flow. A three-way valve was used to alternate HR-ToF-AMS
193 sampling between the above- and below-canopy inlets at 10-minute intervals.

194 2.2.3 PTR-QiToF

195 Above-canopy mixing ratios and fluxes, along with in-canopy vertical gradients, were measured for a wide array of
196 VOCs during PROPHET-AMOS 2016 by Proton Transfer Reaction-Quadrupole interface Time-Of-Flight mass spectrometry
197 (PTR-QiToF). A detailed description of the sampling configuration, calibration and zeroing procedures, humidity
198 corrections, and instrumental performance during the campaign is provided by Alwe et al. (2019) and Millet et al. (2018).
199 Briefly, six identical 45-m inlet lines (0.5" OD/0.375" ID PFA, each heated to 50°C) were installed on the PROPHET tower
200 to sample from 34 m, 21 m, 17 m, 13 m, 9 m, and 5 m above ground level. Sample flow was maintained at ~40 standard
201 L/min (SLM) for the 34 m inlet line and at >5-10 SLM for the others. Each hour, 30 min was spent sampling from the 34 m
202 inlet to quantify above-canopy VOC mixing ratios and fluxes. The remainder of each hour was spent characterizing in-
203 canopy vertical gradients by sequentially sampling from the other inlets (for 5 min apiece) followed by a 5-min instrumental
204 blank.

205 2.3 HR-ToF-AMS data and positive matrix factorization analysis

206 Data analysis for HR-ToF-AMS data was performed in Igor Pro v6.37 using the SQUIRREL v1.57 (SeQUential Igor
207 data RetRiEval) and PIKA v1.16 (Peak Integration by Key Analysis) analysis toolkits. High-resolution mass spectral fitting
208 was performed on HR-ToF-AMS V-mode data. Ratios such as the oxygen-to-carbon elemental ratio (O:C) and hydrogen-to-
209 carbon elemental ratio (H:C) were determined according to the “improved-ambient” (IA) method (Canagaratna et al., 2015).
210 The IA method uses specific ion fragments to correct for compositional biases, and this method has been shown to calculate
211 accurately the elemental ratios of organic laboratory standards that are more representative of oxidized, ambient OA species
212 (Canagaratna et al., 2015). The default values for relative IE were used for each of the following species: OA (1.4), SO₄
213 (1.2), NH₄ (4), NO₃ (1.1), and Chl (1.3), where values in parentheses refer to the ratio of the IE of the given species with
214 respect to the value of IE of NO₃ obtained during routine IE calibrations using NH₄NO₃.

215 To account for the effects of aerosol composition on the transmission efficiency of aerosols to the detection region of the
216 HR-ToF-AMS, a chemical composition-dependent (and therefore time-dependent) collection efficiency (CDCE) was applied
217 to the HR-ToF-AMS data (Middlebrook et al., 2012), which led to a campaign average CDCE of 0.77 +/- 0.18. During the
218 campaign, the HR-ToF-AMS time resolution was 40 seconds from 2 July 02:00 to 19 July 10:00 LT, after which the HR-
219 ToF-AMS time resolution was changed to 30 seconds between 22 July 11:00 and 31 July 15:00 LT (due to instrumental
220 changes after an HR-ToF-AMS power supply failure). Calculated detection limits of NR-PM₁ species are included in Table
221 S3.

222 Positive matrix factorization (PMF) is a mathematical model in which measured data are decomposed into a
223 combination of factors that have varying contributions throughout a time series. Here, the PMF model has been applied to
224 HR-ToF-AMS data to retrieve OA factors that contain information regarding OA sources, chemical properties, and/or
225 atmospheric processing (Jimenez et al., 2009; Ulbrich et al., 2009; Zhang et al., 2011). Subtypes of OA extracted from OA
226 mass spectra using PMF often include (but are not limited to): more-oxidized oxygenated OA (MO-OOA), less-oxidized
227 oxygenated OA (LO-OOA), hydrocarbon-like OA (HOA), biomass burning organic aerosol (BBOA), and cooking organic
228 aerosol (COA) (Cubison et al., 2011; Jimenez et al., 2009; Mohr et al., 2012; Zhang et al., 2007, 2005). The OOA-related
229 factors are generally considered to be associated with SOA, while subtypes such as HOA, BBOA, and COA are presumed to
230 correspond to POA. Factors associated with isoprene-derived epoxydiol OA (IEPOX-OA) have also been identified using
231 PMF using enhanced signals at m/z 82 in their OA mass spectra (Hu et al., 2015). A detailed description of the PMF model
232 (Paatero and Tapper, 1994; Paatero, 1997; Ulbrich et al., 2009; Xu et al., 2015) is included in the SI.

233 The results of the separate PMF analyses on above- and below-canopy OA are included in the SI. For the above-canopy
234 OA data, a summary of the PMF factor selection (Table S4), factor time series correlations with external data (Table S5),
235 factor mass spectra correlations with reference mass spectra (Table S6), time series of PMF model residuals (Figure S4), and
236 mass spectra and time series for possible two- to five-factor PMF solutions (Figure S5 - Figure S8) are shown in the SI.
237 VOCs measured above-canopy via PTR-QiToF at the top of the PROPHET tower are defined in Table S7, and factor time
238 series correlations with the time series of these VOCs are shown in Table S8. PMF diagnostics, such as the mass spectra and
239 time series correlation amongst factors (Figure S9), FPEAK and SEED diagnostic plots (Figure S10), results of the FPEAK
240 analysis (Table S9), model residual diagnostic plots (Figure S11), and results from bootstrapping analysis (Figure S12) are
241 shown in the SI. Finally, Figure S13 displays the time series and high-resolution mass spectra of the optimal solution for the
242 above-canopy OA dataset.

243 For the below-canopy OA data, a summary of the PMF factor selection (Table S10), factor time series correlations with
244 external data (Table S11), factor mass spectra correlations with reference mass spectra (Table S12), mass spectra and time
245 series of possible two- to five-factor PMF solutions (Figure S14 - Figure S17), factor time series correlations with VOCs
246 measured via PTR-QiToF at the 34-m inlet on the PROPHET tower (Table S13), mass spectra and time series correlations
247 amongst factors (Figure S18), FPEAK and SEED diagnostic plots (Figure S19), results from FPEAK analysis (Table S14
248 and Table S15), model residual diagnostic plots (Figure S20), and results from bootstrapping analysis (Figure S21) are

249 shown in the SI. Finally, the time series and high-resolution mass spectra of the optimal three-factor solution for below-
250 canopy OA are shown in Figure S22.

251 2.4 HYSPLIT backward trajectory analysis

252 2.4.1 Trajectory cluster analysis

253 Backward-trajectories are used in this study to determine the origin of air masses arriving at the field site using the
254 Hybrid Single-Particle Lagrangian Integrated Trajectory (HYSPLIT) model (Draxler and Hess, 1998; Stein et al., 2015).
255 Meteorological data from the US Eta data assimilation system archive at 40-km spatial resolution (EDAS40) are used for
256 HYSPLIT trajectory calculations. The EDAS40 data output is constructed using forecasted data from the Eta model, which
257 utilizes observations from surface, aircraft, and satellite data to predict meteorological parameters such as pressure, wind
258 speed, and wind direction (Cooper et al., 2001).

259 In order to assess the influence of air mass histories on aerosols at each site, a cluster analysis was performed on
260 backward trajectories using MeteoInfo v1.4.9R2 and the TrajStat v1.4.4R8 package (Wang, 2014; Wang et al., 2009). The
261 angle distance clustering type is used in this study and calculates the angular distance between two backward trajectories as
262 seen from the site, using methods outlined in Sirois and Bottenheim (1995). The number of suitable clusters is chosen based
263 on the slope of the percentage change in total spatial variation versus number of clusters and a visual inspection of the mean
264 trajectories of the cluster numbers.

265 2.4.2 Weighted potential source contribution function (WPSCF) analysis

266 In addition to a backward-trajectory cluster analysis performed for bulk aerosol properties and gas-phase species, two-
267 day HYSPLIT backward-trajectories initiated from the PROPHET site at 500 m above ground level are used in a weighted
268 potential source contribution function (WPSCF) analysis for OA factors. WPSCF analysis is performed in MeteoInfo
269 v1.4.9R2 using the TrajStat v1.4.4R8 package and results are plotted using ESRI's ArcMap v10.1 (Wang, 2014; Wang et al.,
270 2009). Similar PSCF analyses using backward-trajectories have been performed previously using aerosol properties (Bondy
271 et al., 2017; Chang et al., 2017; Polissar, 1999; Schulze et al., 2018).

272 The number of backward-trajectory endpoints falling within a given grid cell with coordinates (i, j) is defined as n_{ij} .
273 The number of instances in which backward-trajectories ending at a given grid cell have a value (i.e., OA factor mass
274 concentration) higher than an arbitrarily set criterion value is defined as m_{ij} . The PSCF value for a cell at location (i, j) is
275 then defined as follows:

$$276 \text{PSCF}_{ij} = \frac{m_{ij}}{n_{ij}} \quad (1)$$

277 When calculating values of PSCF, some grid cells will contain only a small number of backward-trajectory endpoints. In
278 order to reduce the high uncertainties related to a limited number of endpoints falling within a grid cell in PSCF analysis, a
279 weighting function is applied to the trajectory numbers following the methods of Polissar et al. (2001):

$$280 W_{ij} = \begin{cases} 1.00 & 80 < n_{ij} \\ 0.70 & 20 < n_{ij} \leq 80 \\ 0.42 & 10 < n_{ij} \leq 20 \\ 0.05 & n_{ij} \leq 10 \end{cases} \quad (2)$$

281 In this study, the domain of analysis is set to the geographical extents of the two-day HYSPLIT backward trajectories
282 initiated from the PROPHET site. A grid cell size of 0.5° by 0.5° is used. Median values of the OA factors are used as the
283 arbitrary criterion values. Overall, the WPSCF analysis allows for an identification of potential source areas, where higher
284 WPSCF values within a region indicate a higher likelihood that this region results in observed values higher than the
285 criterion values.

286 2.5 Sonic anemometer data-processing

287 Turbulence measurements during the campaign were obtained from five sonic anemometers installed on the PROPHET
288 tower at the following measurement heights: 34m (CSAT 3B, Campbell Scientific Inc.), 29m (81000, RM Young), 21m
289 (CSAT 3, Campbell Scientific Inc.), 13m (CSAT 3, Campbell Scientific Inc.), and 5m (CSAT 3, Campbell Scientific Inc.).
290 The sonic anemometer at 34 m was operated continuously during the campaign while data are only available from the lower
291 heights from 9 July – 29 July 2016. High-frequency data are de-spiked (data points outside of 3.5-standard deviations are
292 removed) and then separated into 30-minute windows to apply a tilt correction such that the x-axis is rotated into the
293 direction of the mean wind velocity (Foken, 2008). Reynolds decomposition is then applied to the three-dimensional wind
294 components (u, v, w), so each variable (e.g., u) is separated into its mean (\bar{u}) and fluctuating component (u'). The friction
295 velocity, u^* , is defined then as

$$296 \quad u^* = \frac{-\overline{u'w'}}{k} \quad (3)$$

297 Any 30-minute periods that experienced rain (as measured by the rain-gauge at the UMBS AmeriFlux tower), weak winds
298 (winds less than 0.5 m s^{-1} at the top sonic anemometer), or wind directed through the tower were excluded due to potential
299 interference.

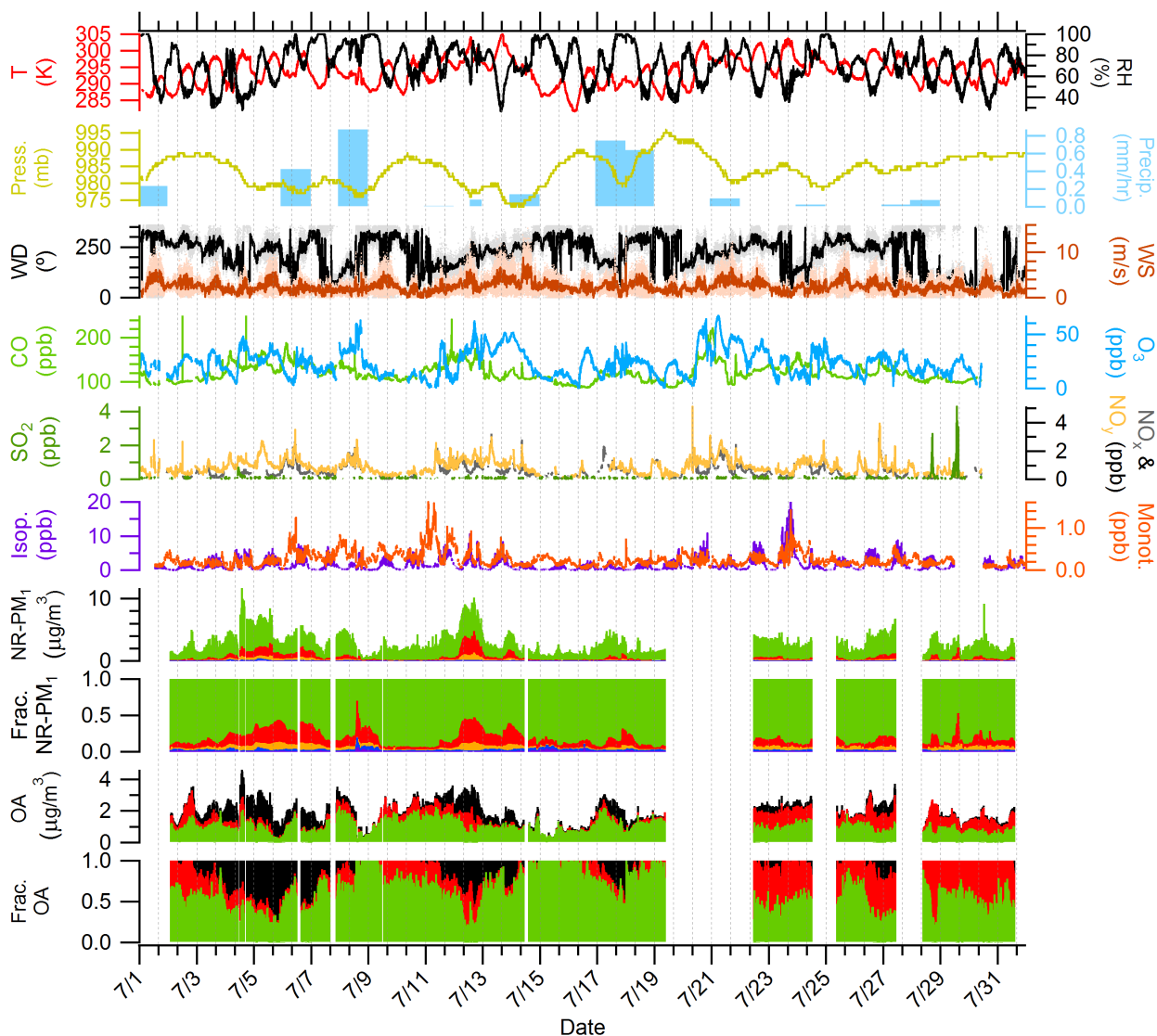
300 3 Results and discussion

301 3.1 Backward-trajectory cluster analysis

302 Two-day backward trajectories are initiated from the PROPHET site and calculated at one-hour intervals from the
303 beginning to the end of the campaign (1 July 00:00 – 31 July 21:00 LT) at 500 meters above ground level, an elevation
304 selected to be within the boundary layer during the day and to avoid trajectory interaction with the surface. A total of 742
305 two-day backward-trajectories are calculated over the course of the campaign. Cluster analysis resulted in three directional
306 clusters: southerly (299 of 742), northeasterly (192 of 742), and northwesterly (251 of 742) (as shown in Figure S23 in the SI
307 as Cluster 1, 2, and 3 respectively). Further description of cluster number selection is discussed in Figure S24 in the SI.
308 Similar to the air mass history analyses at the PROPHET site in Cooper et al. (2001) and VanReken et al. (2015), eight-hour
309 transitional periods between backward-trajectory classifications were removed from analysis because it is likely that the
310 chemical species from these different air masses are mixed. In total, transitional periods composed 22% of the total number
311 of backward-trajectories (165 of 742 total), and the remaining 577 are used for further analysis. Mean values of
312 anthropogenically-influenced species such as SO_4 and benzene were not statistically significantly different ($p < 0.01$)
313 between trajectories from northeasterly and northwesterly clusters, so trajectories from these two clusters are grouped to
314 represent a “northerly” air mass type. During the PROPHET-AMOS study, northerly transport occurred during 60% of the
315 study period (341 of 577), while southerly transport occurred 40% of the time (236 of 577). This type of air-mass
316 classification is consistent with previous summertime studies at the PROPHET site where northerly transport occurred 44%
317 (1998), 60% (2009), and 57% (2014) of the time and southerly transport occurred 24% (1998), 29% (2009), and 43% (2014)
318 of the time (Cooper et al., 2001; Gunsch et al., 2017; VanReken et al., 2015).

319 3.2 Non-refractory submicron time series and bulk chemical composition

320 Figure 1 shows the time series of the mass concentrations of OA, SO_4 , NH_4 , NO_3 , and Chl as measured by the HR-ToF-
321 AMS. Mass concentrations plotted in Figure 1 represent time series data from both the above- and below-canopy sampling
322 inlets. The average total NR- PM_{10} (sum of mass concentrations of OA, SO_4 , NH_4 , NO_3 , and Chl) is $2.3 \pm 1.5 \mu\text{g m}^{-3}$. High
323 NR- PM_{10} concentration episodes (7/3-7/7 and 7/11-7/14) are strongly influenced by southerly air masses advecting



324
 325 **Figure 1: Overview of time series of the following from top to bottom: temperature (T) and RH; pressure (Press.)**
 326 **and precipitation (Precip.); wind direction (WD) and wind speed (WS); CO and O₃; SO₂, NO_x, and NO_y; isoprene**
 327 **(Isop.) and total monoterpenes (Monot.); particulate OA (green), NO₃ (blue), SO₄ (red), NH₄ (orange), and Chl**
 328 **(purple); fraction of species to total NR-PM₁, OA factors derived from PMF, and fractional contribution of OA**
 329 **factors to total OA. OA factors are colored as follows: MO-OA (black), IEPOX-OA (red), and 91Fac (green).**
 330 **Precipitation data are provided from the NADP site in Cheboygan County, MI. Trace gas data (CO, O₃, SO₂, NO_x,**
 331 **and NO_y) are measured from the 6-m inlet on the MAQL. Meteorological data (T, RH, Press., WD, and WS) and**
 332 **VOC data (Isop. and Monot.) are measured from the 34-m inlet on the PROPHET tower. The OA time series include**
 333 **data from both heights (6 m and 30 m), with the sampling switched at 10-minute intervals.**

334
 335 to the site, as confirmed by the HYSPLIT backward-trajectory clusters shown in Figure S23 in the SI. Northerly backward-
 336 trajectories originated over clean, remote areas in Canada, while southerly backward-trajectories originated over more
 337 anthropogenically influenced areas. OA is the dominant NR-PM₁ component over the entire campaign, representing

338 approximately 84.2% of the NR-PM₁ mass. SO₄ contributes the second highest average mass fraction to NR-PM₁ (10.7%)
339 followed by NH₄ (3.1%), NO₃ (1.6%), and Chl (0.4%). During periods of northerly flow, OA represents 89.5% of the
340 average NR-PM₁ mass, while SO₄, NH₄, NO₃ and Chl represent 6.9%, 1.9%, 1.3%, and 0.4%, respectively. Periods of
341 southerly flow decrease the relative contribution of OA to 75.5% and Chl to 0.3% while increasing the relative contribution
342 of SO₄ to 16.8%, NH₄ to 5.6%, and NO₃ to 1.3%. The increased fractional contribution of OA during periods of northerly-
343 originating air is consistent with results from VanReken et al. (2015), who found that water-soluble organics dominated
344 aerosol mass during periods of “clean” northerly flow at the PROPHET site. Sheesley et al. (2004) also found the aerosol
345 organic carbon composition at a remote site in the upper peninsula of Michigan (approximately 100 miles from the
346 PROPHET site) was greatly influenced by the source region of the air parcel. This study found that both stagnant and
347 northerly air parcels contained higher concentrations of pinonic acid and limited amounts of primary emission tracer
348 compounds, while anthropogenically influenced air parcels from the south and northwest contained higher concentrations of
349 aromatic and aliphatic dicarboxylic acids.

350 Diurnal plots for OA, SO₄, NH₄, NO₃, O:C, and H:C are shown in Figure S25 in the SI. The diurnal profiles of OA,
351 SO₄, and NH₄ are all relatively flat and do not have a clear diurnal trend. The lack of clear diurnal variations for SO₄ is
352 consistent with regional transport as the source of SO₄ during this campaign. The diurnal variations of NO₃ show increases
353 in the morning, with a maximum around approximately 10:00 local time, and lower concentrations in the afternoon.

354 Using the backward-trajectory clustering results described in Section 3.1, mean values of NR-PM₁, NR-PM₁ species, OA
355 elemental ratios, meteorological parameters, and trace gases for the entire campaign, northerly, and southerly backward-
356 trajectory clusters are shown in Table 1. Overall, relative to northerly air masses, southerly air masses were found to be
357 warmer (~2 °C), more humid (~5%), and associated with higher concentrations of NO_x, NO_y, O₃, and benzene. Furthermore,
358 on average, southerly air masses had higher concentrations of NR-PM₁, OA, SO₄, NH₄, and NO₃. Higher levels of OA
359 oxidation (8% difference) based on O:C are also observed during periods of southerly flow (O:C = 0.69 versus 0.75 for
360 northerly versus southerly flow, respectively). An additional metric of oxidation, the oxidation state of carbon (OSc),
361 indicates that the degree of oxidation is higher during periods of southerly flow (OSc = -0.12 versus 0.06 for northerly versus
362 southerly flow, respectively, where $OSc = 2 * O:C - H:C$) (Kroll et al., 2011). The factor of 5 differences between northerly
363 and southerly SO₄ is consistent with the increased influence of SO₂ point sources from electric-generating units south of the
364 site in Ohio, Indiana, and Illinois. Overall, these observations demonstrate that anthropogenic influence from southerly flow
365 directly affects NR-PM₁ mass concentrations, NR-PM₁ composition, the degree of OA oxidation, and trace gas mixing ratios
366 at this site. Results are in agreement with VanReken et al. (2015), where southerly air masses or those “anthropogenically
367 impacted” were found to contain higher aerosol loadings (in terms of aerosol volume, particle number, and median particle
368 diameter) and hygroscopicity, along with increased trace gases abundances, as compared to northerly air masses or “clean”
369 regimes.

370 Oxygen-containing ion families (C_xH_yO_zz₁⁺) represent over 50% of the campaign-averaged OA high-resolution mass
371 spectrum, and this high degree of oxygenation is reflected in an average O:C ratio of 0.71 +/- 0.08 and an average H:C ratio
372 of 1.49 +/- 0.06. A distinct peak at m/z 44 in the average mass spectrum accounts for 14.1% of the total OA. The peak at
373 m/z 44 is mainly composed of the CO₂⁺ ion (96.0% of m/z 44). The ratio of m/z 44 to the total signal in the organic mass
374 spectrum (f₄₄), a surrogate for O:C and an indicator for photochemical aging, in this study is 0.14. Together with the average
375 O:C ratio (0.71) observed in this study, these values are consistent with OOA observed across AMS datasets (Jimenez et al.,
376 2009; Ng et al., 2010). Other prominent ions in the campaign-averaged high-resolution mass spectrum include m/z 55, 82,
377 and 91. Fragments at m/z 55 represent 2.4% of the total OA, and are representative of both oxygenated and hydrocarbon
378 fragments, such as C₃H₃O⁺ (50.2% of m/z 55) and C₄H₇⁺ (42.9% of m/z 55). The possible OA sources leading to increased
379 signal at m/z 82 (0.46% of total OA) and 91 (0.62% of total OA) will be discussed in the following section. Figure S25
380 in the SI shows the diurnal variations of O:C and H:C, indicating relatively stable diurnal cycles. Increases in H:C are observed
381 starting at 9:00 before reaching a maximum at midday (13:00) followed by a slow decrease between the hours of 13:00 and
382 20:00, while an opposite pattern is observed for mean values of O:C.

383

384 **Table 1: Campaign-averaged values (+/- one standard deviation from the mean) of mass concentrations of NR-PM₁, VOC and**
 385 **trace gas mixing ratios, and meteorological parameters, as well as hourly-averaged values associated with northerly and southerly**
 386 **backward-trajectory clusters. Northerly and southerly air masses are defined in Section 3.1 using a cluster analysis of HYSPLIT**
 387 **two-day backward trajectories.**

Parameter	Campaign	Northerly	Southerly
NR-PM ₁ (μg m ⁻³)	2.3 ± 1.5	1.8 ± 0.7	3.6 ± 2.0
OA (μg m ⁻³)	1.9 ± 1.0	1.6 ± 0.6	2.6 ± 1.3
SO ₄ (μg m ⁻³)	0.3 ± 0.4	0.1 ± 0.1	0.7 ± 0.6
NH ₄ (μg m ⁻³)	0.1 ± 0.1	0.04 ± 0.04	0.2 ± 0.2
NO ₃ (μg m ⁻³)	0.04 ± 0.03	0.02 ± 0.01	0.06 ± 0.05
Chl (μg m ⁻³)	0.01 ± 0.00	0.01 ± 0.00	0.01 ± 0.00
O:C	0.7 ± 0.1	0.7 ± 0.1	0.8 ± 0.1
H:C	1.5 ± 0.1	1.5 ± 0.0	1.4 ± 0.00
OSc	-0.1 ± 0.2	-0.1 ± 0.1	0.1 ± 0.2
Isoprene (ppb) ^{a, b}	1.6 ± 1.9	1.5 ± 1.5	1.8 ± 1.5
Monoterpenes (ppb) ^{a, b}	0.3 ± 0.2	0.2 ± 0.1	0.2 ± 0.2
Benzene (ppb) ^a	0.04 ± 0.02	0.03 ± 0.01	0.05 ± 0.02
NO (ppt) ^c	24.1 ± 36.4	21.5 ± 16.2	29.7 ± 29.5
NO ₂ (ppt) ^c	593.0 ± 445.8	369.4 ± 257.7	872.0 ± 478.6
NO _y (ppt) ^c	934.5 ± 490.0	610.5 ± 271.8	1283.9 ± 412.6
O ₃ (ppb) ^c	24.1 ± 11.9	20.1 ± 8.3	30.5 ± 13.2
CO (ppt) ^c	120.6 ± 21.5	109.6 ± 12.6	134.7 ± 21.7
SO ₂ (ppb) ^{b, c}	31.3 ± 174.2	45.0 ± 212.0	23.1 ± 64.2
Temperature (°C) ^c	20.6 ± 4.6	20.3 ± 4.5	22.4 ± 4.5
Relative Humidity (%) ^c	73.8 ± 17.3	68.6 ± 17.0	73.5 ± 17.6

388 ^a VOC measurements using University of Minnesota's PTR-QiToF from the 34-m inlet on the PROPHET tower.

389 ^b Table entries where the differences between the northerly and southerly backward-trajectories mean values are not
 390 statistically significant ($p < 0.01$) using a two-sample t-test.

391 ^c Trace gas and meteorological parameters measured from onboard the MAQL.

392

393 3.3 Organic aerosol source apportionment

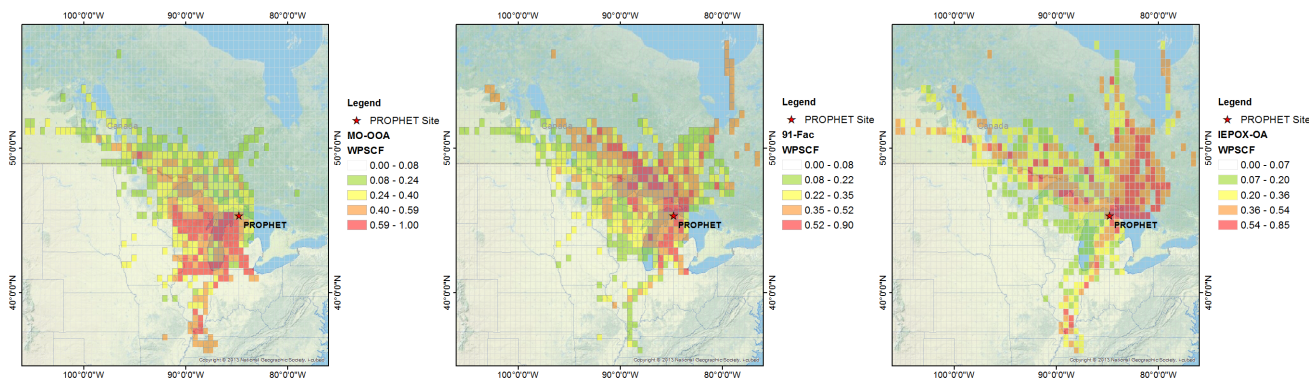
394 A three-factor solution is obtained for both the above-canopy inlet at 30 meters above the UMBS forest floor (A-MO-
 395 OOA, A-IEPOX-OA, A-91Fac) and the below-canopy inlet at 6 meters within the UMBS canopy (B-MO-OOA, B-IEPOX-
 396 OA, and B-91Fac). The 91Fac factor represents OA with enhanced signal at m/z 91 in the mass spectrum. The addition of
 397 more factors to the PMF solution beyond three factors resulted in less physically meaningful and interpretable factors. Thus,
 398 the three-factor solution is considered the optimal solution for the above- and below-canopy OA datasets. In this study, seed
 399 = 0 was chosen for both PMF solutions as there was minimal variation in Q/Q_{exp} across the 50 seeds. Solutions at $FPEAK =$
 400 0 were chosen because solutions at other $FPEAK$ values did not present improved correlations between factors and reference
 401 mass spectra.

402 Time series of mass concentrations and time series of fractional contributions to total OA are shown in Figure 1. The
 403 O:C ratio of each of the OA factors are as follows: 0.65 (IEPOX-OA), 0.71 (91Fac), and 0.89-0.90 (MO-OOA), all of which
 404 indicate the high degree of oxygenation in each of the factors. For the above-canopy PMF solution, 91Fac makes the largest

405 contribution to the total OA (43.8%), followed by IEPOX-OA (32.8%) and MO-OOA (23.4%). For the below-canopy PMF
406 solution, 91Fac also makes the largest contribution to the total OA (42.5%), followed by IEPOX-OA (34.0%) and MO-OOA
407 (23.5%). Details on the chemical composition, mass spectral characteristics and diurnal profiles of each factor are discussed
408 further in the SI.

409 Hourly averages of the above-canopy OA factors are paired with hourly two-day backward-trajectories for WPSCF
410 analysis. Results from WPSCF analysis using above-canopy OA data (Figure 2) indicate that A-MO-OOA predominantly
411 originates from southerly air masses, as supported by external measurements data such as benzene, OVOCs, carbonyls, and
412 SO₄. Air masses that originate from the south pass over the large urban centers of Chicago, Milwaukee, and Detroit. This
413 further supports the aged, transported nature and anthropogenic influences of the observed A-MO-OOA at this site. In
414 contrast, no strong indication of a distinct source region is observed for 91Fac. This could suggest a more localized source
415 of 91Fac in relation to the site. Combining these WPSCF results with correlations of 91Fac with VOC masses corresponding
416 to monoterpene oxidation suggests that 91Fac is sourced from local biogenic, monoterpene-oxidation related chemistry (Xu
417 et al., 2018). Finally, WPSCF results for A-IEPOX-OA indicate that this OA factor coincides with more northerly airflow
418 with some contributions from northwesterly flow. These northerly source regions driving A-IEPOX-OA correspond to more
419 rural, less anthropogenically influenced locations in Canada. Interestingly, an instance of high WPSCF values for A-
420 IEPOX-OA and A-MO-OOA can be traced back to areas near the southeastern tip of Missouri and western Tennessee,
421 implying long-range transport of these OA factors. Backward-trajectories associated with this instance of high WPSCF
422 values for IEPOX-OA pass over areas in the high isoprene-emitting region in the Ozarks of southern Missouri, which is
423 commonly referred to as the “isoprene volcano” (Carlton and Baker, 2011; Wiedinmyer et al., 2005). The median mass
424 concentrations of above-canopy OA factors used as the criterion values for the WPSCF method were A-MO-OOA: 0.31 $\mu\text{g m}^{-3}$,
425 A-91Fac: 0.68 $\mu\text{g m}^{-3}$, and A-IEPOX-OA: 0.58 $\mu\text{g m}^{-3}$. Overall, WPSCF analysis indicates that transport from southerly
426 flow (A-MO-OOA), local sources (A-91Fac), and transport from northerly flow (A-IEPOX-OA) are related to the OA
427 factors observed at this site.

428



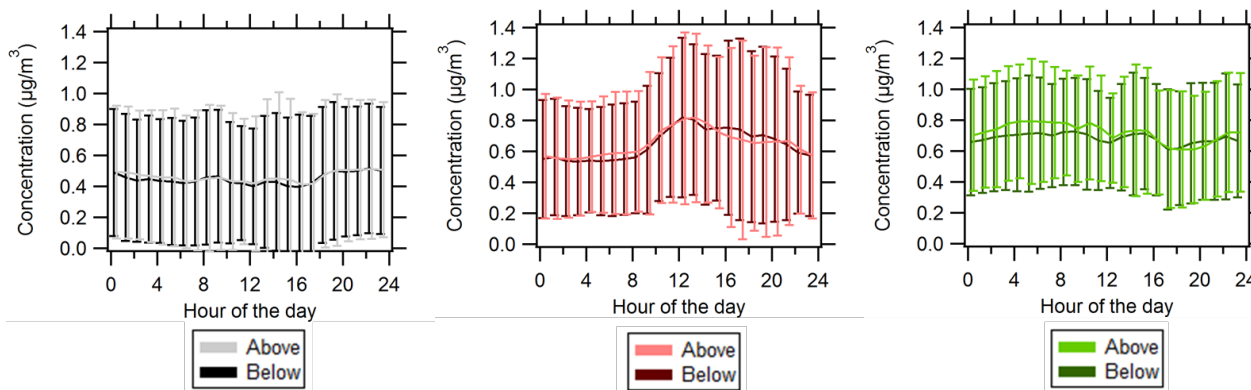
429

430 **Figure 2: WPSCF backward-trajectory analysis maps for the following hourly-averaged OA factors from left to right: above-**
431 **canopy MO-OOA, above-canopy 91Fac and above-canopy IEPOX-OA. The geographical location of the PROPHE'T site is**
432 **represented by a red star. WPSCF analysis is performed using HYSPLIT two-day backward trajectories, a grid cell size of 0.5° by**
433 **0.5°, and the geographical domain of the extents of the two-day backward trajectories. Median mass concentrations of above-**
434 **canopy OA factors (A-MO-OOA: 0.31 $\mu\text{g m}^{-3}$, A-91Fac: 0.68 $\mu\text{g m}^{-3}$, and A-IEPOX-OA: 0.58 $\mu\text{g m}^{-3}$) are used as the criterion**
435 **WPSCF values. Color scales correspond to probability of source regions for each respective OA factor, and it should be noted that**
436 **the range and gradation of the color scale changes between each plot. Map was generated using ArcMap10.1 using the 2013**
437 **National Geographic Society, i-cubed basemap.**

438

439 Overall, PMF analysis for both sampling inlets at the site indicates that the OA is a combination of MO-OOA, 91Fac,
440 and IEPOX-OA. The dominant OA factor is 91Fac, and during periods of southerly flow MO-OOA contributes relatively

441 more (time series of the fractional contributions to total OA shown from both inlets is shown in Figure 1 and is also shown
 442 separately for each inlet in Figure S13 and Figure S22 in the SI). On average, source apportionment results indicate that the
 443 OA at both inlets generally had similar average fractional OA contributions and degrees of oxidation. Diurnal profiles for
 444 above- and below-canopy OA are shown in Figure 3 and indicate that diurnal profiles and variations are similar between the
 445 two inlets for each OA factor. It is worth noting the diurnal pattern of the IEPOX-OA factor, likely indicating a relatively
 446 small influence of local isoprene emissions.
 447



448
 449 **Figure 3: Diurnal profiles of (left) MO-OOA, (middle) IEPOX-OA, and (right) 91Fac where solid lines represent average values**
 450 **and whiskers represent one standard deviation from the mean. Darker colors represent below-canopy OA (B-MO-OOA, B-**
 451 **IEPOX-OA, B-91Fac) while lighter colors represent above-canopy OA (A-MO-OOA, A-IEPOX-OA, A-91Fac). Data for below-**
 452 **canopy OA factors have been offset by 15 minutes simply to aid plot interpretation.**

453
 454 **3.4 Vertical characterization of above- and below-canopy NR-PM₁ and OA factors**

455 **3.4.1 Similarity between above- and below-canopy environments**

456 Mean values of NR-PM₁, NR-PM₁ species, OA elemental ratios, meteorological parameters, VOCs, and trace gases from
 457 the above- and below-canopy inlets are summarized in Table 2. Each of the mean values for the parameters listed in Table 2
 458 are within one standard deviation of each other for the below- and above-canopy sampling heights. However, results from
 459 Wilcoxon rank-sum tests indicate that the medians for a majority of the above- and below-canopy parameters are
 460 significantly different ($p = 0.05$). To provide a comparison of the two inlets on the same time scale, scatter plots of 30-
 461 minute averaged values are shown in Figure 4 for OA factors, total OA, SO₄, and O:C. For reference, a 1:1 line is shown on
 462 each scatter plot. Values falling within one standard deviation are similar between above and below canopy, while values
 463 deviating farther from the 1:1 line indicate values in which the above- or below-canopy environment had differing
 464 concentrations. Figure 4 illustrates that mass concentrations of OA factors, total OA, and SO₄ were similar over a majority
 465 of the campaign and suggests that the above- and below-canopy environments were generally coupled from a PM
 466 perspective. It also appears that total OA, MO-OOA, IEPOX-OA, and 91Fac show increases above canopy relative to below
 467 canopy at the highest end of the range of the measurements.

468 Results from a recent study from the PROPHET-AMOS 2016 campaign by Millet et al. (2018) indicate that flux of
 469 isoprene and monoterpenes at the canopy-atmosphere boundary represents over half of the net carbon flux, while OVOCs
 470 constitute a majority of the species with detectable VOC fluxes. Overall, the authors report that the observed and modeled
 471 net carbon flux during the campaign was upward (canopy emission) during the campaign in 2016. Additionally, in-canopy
 472 gradients of directly emitted BVOCs, such as isoprene and monoterpenes, indicate patterns that are consistent with their
 473 respective temperature, light, and physical emission dependencies (higher concentrations in-canopy for isoprene and higher

474 in the lower canopy for monoterpenes). On the other hand, in-canopy gradients of secondary products from BVOC
 475 oxidation, such as acetic acid and glycoaldehyde, indicate patterns consistent with net nighttime uptake and a weak peak
 476

477 **Table 2: Campaign-averaged values (+/- one standard deviation) of mass concentrations of NR-PM₁, VOC and trace gas mixing**
 478 **ratios, and meteorological parameters above and below the canopy.**

Parameter ^{a, b}	Above	Below
NR-PM ₁ (μg m ⁻³)	2.4 ± 1.6	2.3 ± 1.5
OA (μg m ⁻³)	1.9 ± 1.0	1.8 ± 1.0
SO ₄ (μg m ⁻³)	0.3 ± 0.5	0.3 ± 0.4
NH ₄ (μg m ⁻³)	0.1 ± 0.2	0.1 ± 0.2
NO ₃ (μg m ⁻³)	0.04 ± 0.04	0.04 ± 0.03
Chl (μg m ⁻³)	0.01 ± 0.00	0.01 ± 0.00
O:C	0.7 ± 0.1	0.7 ± 0.1
H:C ^c	1.5 ± 0.1	1.5 ± 0.1
OSc	0.0 ± 0.2	-0.1 ± 0.2
Isoprene (ppb)	1.6 ± 1.9	1.8 ± 2.2
Monoterpenes (ppb)	0.3 ± 0.2	0.3 ± 0.3
Benzene (ppb)	0.04 ± 0.02	0.04 ± 0.02
NO (ppt)	36.0 ± 56.9	24.1 ± 36.4
NO ₂ (ppt)	564.8 ± 393.2	593.0 ± 448.8
O ₃ (ppb)	32.2 ± 12.2	24.1 ± 11.9
Temperature (°C) ^c	20.7 ± 4.1	20.6 ± 4.6
Relative Humidity (%)	71.5 ± 17.3	73.8 ± 17.3

479 ^a Summary statistics for NR-PM₁ measurements were calculated using 5-minute averaged data, VOC measurements using 1-
 480 minute averaged data (University of Minnesota's PTR-QiToF 5-m inlet and 34-m inlet), NO_x above-canopy measurements
 481 using 5-minute averaged data (University of Toronto), NO_x and O₃ below-canopy measurements using 5-minute averaged
 482 data (MAQL), and O₃ 1-minute averaged data (CU-Boulder's 27-m inlet on the AmeriFlux Tower).

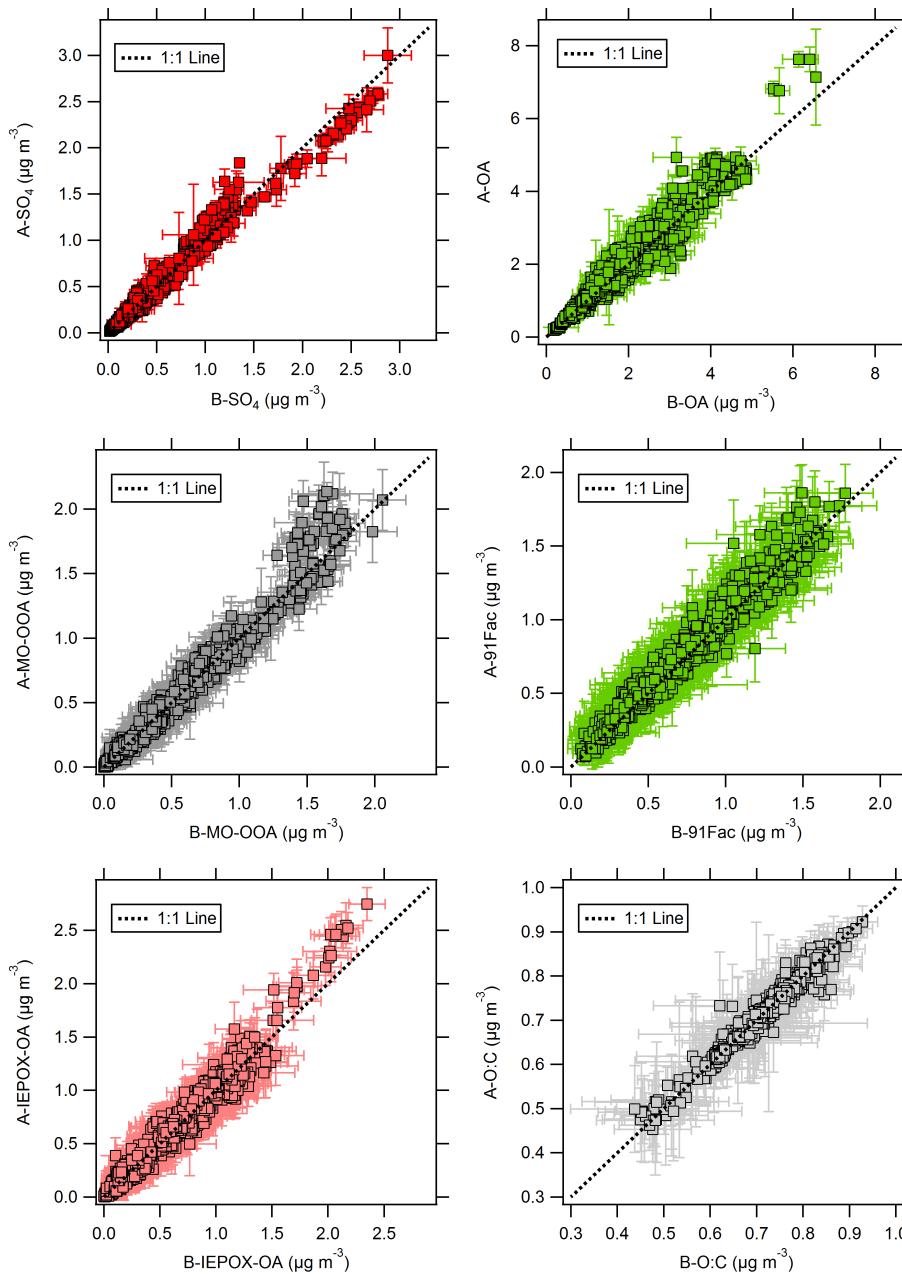
483 ^b Percent of data below detection limit for NR-PM₁: NH₄ (4% / 4%) and Chl (59% / 63%), VOCs: isoprene (30% / 30%),
 484 monoterpenes (56% / 36%), benzene (100% / 100%), and NO (37% / 22%), where percentages are shown for above- and
 485 below-canopy data, respectively. Unless otherwise stated, the percentage below detection limit for all other parameters is
 486 0%.

487 ^c Table entries where the null hypothesis ("equal medians") between the above- and below-canopy data cannot be rejected
 488 and was not statistically significant (p > 0.05) using a two-sided, non-parametric Wilcoxon rank-sum test. All other table
 489 entries indicate that the null hypothesis ("equal medians") can be rejected at the statistical significance level (p < 0.05).
 490

491 concentration near the mid-canopy. Correlation analysis of these secondary oxidation products and HCOOH indicates that
 492 HCOOH likely originates from a secondary source in this environment (Alwe et al., 2019). In the present study, the overall
 493 homogeneity in OA factors implies that, despite vertical gradients in trace gases and BVOCs from primary emission and
 494 secondary production, turbulent mixing of aerosols between the forest canopy and the atmosphere is efficient.

495 Furthermore, this similarity between the above- and below-canopy environments suggests that the chemical timescales
 496 of SOA formation processes likely are long relative to residence times due to turbulent mixing (Foken et al., 2012), assuming
 497 relatively constant background levels. Ultimately, the observed similarity agrees with previous modeling work that predicts
 498 similar SOA mass loadings at these two heights (Ashworth et al., 2015; Schulze et al., 2017). The results shown in the
 499 present work also are in agreement with measurements at the site in 2009, showing that aerosol gradients on the PROPHET

500 tower “existed at times between the above-canopy (31.4m) and understory environments (5 m),” but that the understory
501 conditions were generally similar to that of the above-canopy conditions (VanReken et al., 2015). The vertical similarity in
502



503

504

505

506 **Figure 4: Scatter plots of above- (A) and below- (B) canopy hourly-averaged values for: (top from left to right) SO₄**
507 **and total OA, (middle from left to right) MO-OOA and 91Fac, and (bottom) IEPOX-OA and campaign O:C. The**
508 **three-way valve switched between the two inlets at 10-minute intervals, so 30-minute averaged mass concentrations**
509 **allows for a comparison of both inlets on the same time basis. Above-canopy values are plotted on the y-axis of each**
510 **plot and below-canopy values are plotted on the x-axis of each plot. Averages are shown with squares; whiskers**

511 represent one standard deviation from the mean. For reference, a 1:1 line is shown with each plot. Outliers on the
512 O:C plot corresponding to periods of precipitation were removed.

513

514 NR-PM₁ is also in agreement with findings in the Amazon forest, where a balance between upward and downward fine
515 particle fluxes was found (Rizzo et al., 2010) and in a southeast Asian rainforest, where PM₁ did not show significant
516 variations with height during the daytime (Whitehead et al., 2010).

517 3.4.2 Episodes of vertical differences in NR-PM₁

518 Episodes of vertical differences in NR-PM₁ between the two inlets were observed, and four such episodes are described
519 here: Episode #1 (Period: 7/3/2016 19:30 to 7/5/2016 15:00 LT), Episode #2 (11 July 15:00 to 12 July 23:00 LT), Episode
520 #3 (7/16/2016 21:30 to 7/19/2016 08:30 LT), and Episode #4 (7/26/2016 08:30 to 7/31/2016 13:30 LT). Episodes were
521 defined as sustained periods in which a vertical difference in OA or SO₄ was greater than or equal to concentrations
522 representing $\geq 25\%$ of the campaign averaged OA or SO₄. The “vertical difference,” symbolized as Δ in Figure 5, is defined
523 as the difference between above- and below-canopy values, where the positive convention indicates larger concentrations
524 above the canopy. Episodes #1, #3, and #4 indicate increased above-canopy OA concentrations, while Episode #2 indicates
525 increased below-canopy SO₄ concentrations. Episodes with higher above-canopy NR-PM₁ ranged up to $\sim 1.0 \mu\text{g m}^{-3}$ higher
526 in OA and $\sim 0.5 \mu\text{g m}^{-3}$ higher in SO₄ relative to equivalent above/below mass ($\Delta = 0$). Figure 5 shows time series of vertical
527 differences in OA factors and SO₄ and estimates of friction velocity (u^*) at five different heights (not equal to those for the
528 VOC measurements) on the PROPHET tower over the campaign. Calculated from three-dimensional wind velocity data, u^*
529 is a function of the shear stress at the surface and is used in this study as a metric of in-canopy mixing (Equation 5).

530 The sum of the delta values for each OA factor ($\sum\Delta\text{OA Factors}$) for the episodes are shown in Figure 6 with
531 corresponding observations of u^* and vertical differences in SO₄ and O₃. Figure 6 shows that vertical differences in OA
532 correlate with vertical differences in SO₄ for Episodes #1 and #4, while $\sum\Delta\text{OA Factors}$ during Episode #3 coincides with
533 higher above-canopy O₃ concentrations. Correlations between chemical species for Episode #2 are weaker. Correlation
534 coefficients (r) for each episode are 0.69 (Episode #1 $\sum\Delta\text{OA Factors}$ -Sulfate), -0.44 (Episode #2 Sulfate- u^*), 0.34 (Episode
535 #3 $\sum\Delta\text{OA Factors}$ -Ozone), and 0.59 (Episode #4 $\sum\Delta\text{OA Factors}$ -Sulfate). These episodes have different OA factor
536 composition: MO-OOA contributing a larger percentage during Episode #1 and #2, 91Fac contributing roughly half in
537 Episode #3, and IEPOX-OA contributing more than half of the total OA vertical difference in Episode #4.

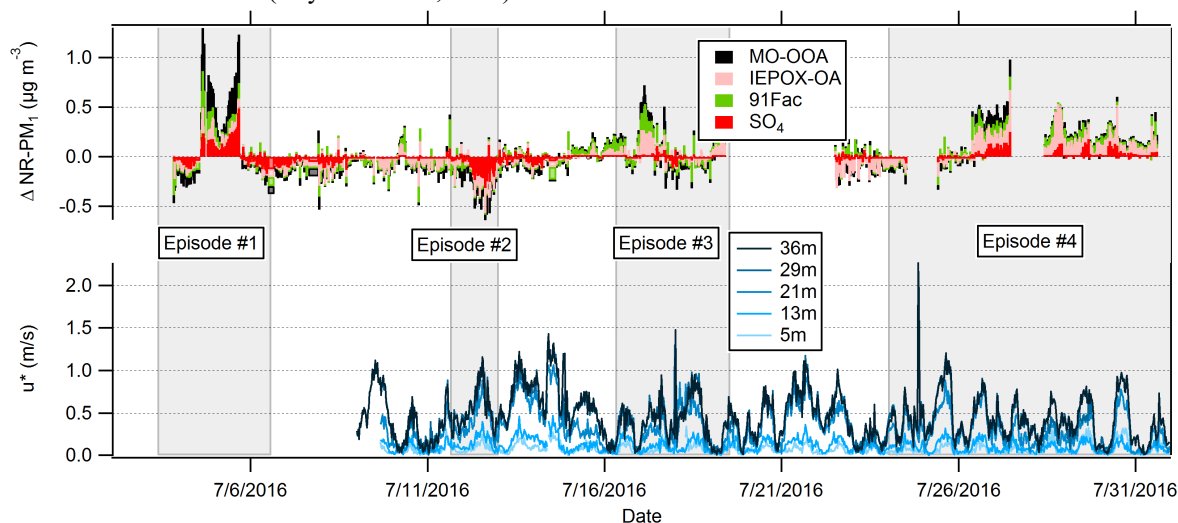
538 3.5 The role of mixing and particulate SO₄ in vertical differences in OA

539 The diurnal profile of vertical difference episodes for total OA, SO₄, and OA factors in 2016 indicate there is no clear
540 diurnal pattern observed for any of these species (Figure S26 in the SI). Maximum vertical differences for SO₄, total OA,
541 and MO-OOA are observed around 3PM. For total OA, a gradual increase occurs at 9AM before reaching a maximum
542 vertical difference at 3PM, suggesting that the episodes of higher above-canopy NR-PM₁ begin shortly after the most
543 common observed hours of canopy uncoupling from the site in 2009. The initiation of these events may also be attributed to
544 venting of the nocturnal boundary layer as it breaks up in the morning hours, as observed for events of upward particle
545 number fluxes by Whitehead et al. (2010).

546 To assess the agreement between the occurrence of episodes and micrometeorological measurements of in-canopy
547 mixing, episode-specific data for Episodes #2-4 are shown in Figure 6. During Episode #1, u^* data are available only at
548 36m, so no friction velocity data are shown, preventing a full analysis similar to those performed for the other three episodes.
549 However, based on similarity in sulfate enhancements, it can be assumed that Episode #1 is somewhat similar to Episode #4.

550 During Episode #2, based on the backward trajectory cluster analysis shown in Table 1 and the WPSCF results, regional
551 transport is the likely source of the PM, including the enhancements below canopy. Prior to this episode, SO₄ and MO-OOA
552 are uniform from below-to-above canopy. The below-canopy enhancement then reaches up to $0.3 \mu\text{g m}^{-3}$ of SO₄.

553 Downmixing of clean air from aloft could lead to lower concentrations above canopy, meaning that the observed difference
 554 would be caused by decreasing above-canopy concentrations, not increasing below-canopy concentrations. However,
 555 below-canopy concentrations are observed to increase while above-canopy concentrations decrease. Without a local, below-
 556 canopy source, this indicates that pollutants from above canopy are mixed into the below-canopy region at a rate faster than
 557 they are lost to deposition. Regional pollutants, advected to the site above the boundary layer, can be mixed down to the
 558 surface with daytime boundary layer growth, as has been found in previous aircraft campaigns (Berkowitz et al., 1998;
 559 Thornberry et al., 2001). Downward transport of air masses from the surrounding region has also been hypothesized to
 560 contribute to higher ratios of organic nitrogen to organic carbon ratios in water-soluble aerosols within a forest canopy
 561 relative to its forest floor (Miyazaki et al., 2014).

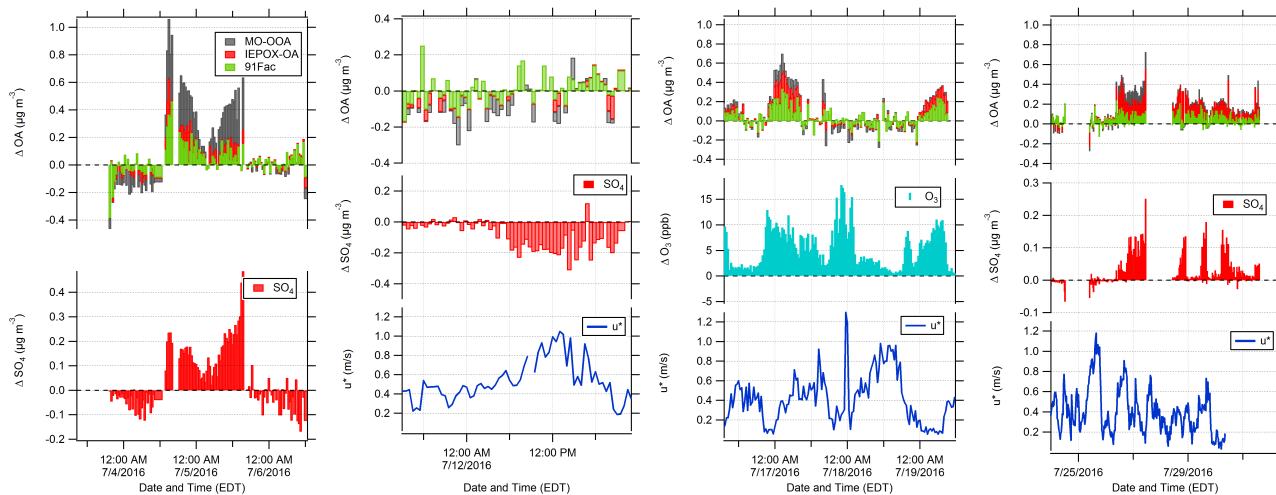


562
 563 **Figure 5: Time series of (top) observed NR-PM₁ vertical differences between above- and below-canopy inlets and**
 564 **(bottom) friction velocity (u^*) in m/s at five different heights on the PROPHET tower. Vertical differences are**
 565 **defined as Δ Species, where Δ refers to the Above-Canopy minus the Below-Canopy mass concentration. Note that**
 566 **the elevations for u^* are slightly different than those for trace gas sampling.**
 567

568 During Episodes #3 and #4, periods of above-canopy enhancement in OA factors coincide with relatively lower u^* ($u^* <$
 569 0.2 m/s during Episode #3 and $u^* < 0.6$ m/s during Episode #4, with the average u^* considering all heights over the duration
 570 of the episode), with lower friction velocities and greater above-canopy enhancement in Episode 3. In the case of Episode
 571 #3, lower in-canopy mixing, mostly occurring during nighttime, agrees well with periods of higher above-canopy OA factor
 572 and O_3 concentrations. In this case, both IEPOX-OA and 91Fac contribute to the OA enhancement, likely due to strong
 573 photochemistry both locally and during transport (as indicated by increased O_3). Episode #4 is the longest duration episode;
 574 however, the agreement between low-mixing and above-canopy PM enhancements is more variable during this case. Similar
 575 to Episode #3, the lowest values of friction velocity occur during the nighttime or early morning. Despite the temporal
 576 misalignment of Δ OA and low u^* , it should be noted that friction velocities lower than the campaign average (~ 0.4 m/s) are
 577 observed during the latter periods of Episode #4 (7/28-7/30), which is consistent with the low mixing hypothesis presented
 578 for Episode #3. Therefore, it appears that stagnant conditions above the canopy created an environment where canopy
 579 exchange became limited and air masses did not fully penetrate into the canopy; aerosol deposition below canopy potentially
 580 enhanced the positive delta values. This scenario could also promote in-canopy OA accumulation, but this does not appear
 581 to have occurred, implying that other factors contributed to these vertical differences. Instead, it appears that increased
 582 sulfate loading was associated with this transport and that this increased sulfate above the canopy led to enhancements above

583 canopy, particularly of IEPOX-OA relative to 91Fac, as shown in Figure 6. This also could be related to associated changes
584 in aerosol liquid water.

585



586

587 **Figure 6: Time series of observed NR-PM₁ vertical difference episodes: (from left to right) Episode #1, Episode #2,**
588 **Episode #3, and Episode #4. Data shown for Episode #1, Episode #2, and Episode #4 include vertical differences in**
589 **30-minute averaged above- and below-canopy SO₄, while data shown for Episode #3 show vertical differences in 30-**
590 **minute averaged above- and below-canopy O₃. The O₃ data were measured from the AmeriFlux Tower at 6 meters**
591 **and 27 meters and were provided courtesy of CU-Boulder. Friction velocity measurements at 29m on the PROPHET**
592 **tower are also provided for Episodes #2-4.**

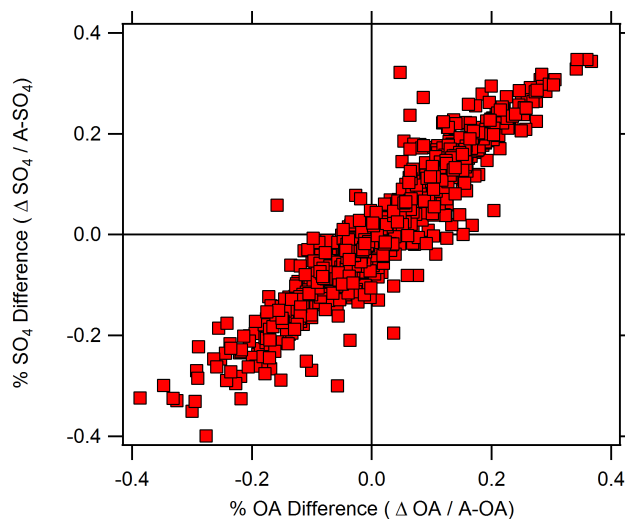
593

594 The probability distributions of ΔSO_4 and ΔO_3 between episodes and the average for the entire PROPHET campaign are
595 compared in Figure S27 of the SI. The cumulative distribution function (CDF) for ΔSO_4 indicates that Episodes #1 and #4
596 had higher probabilities of positive ΔSO_4 (denoting higher above-canopy concentrations), while Episode #2 had higher
597 probabilities of negative ΔSO_4 (denoting higher below-canopy concentrations). The episode-specific CDFs for #1 and #2 are
598 also different from the total campaign CDF, implying that the vertical differences observed were distinct events. The
599 average O₃ difference between the 6- and 27-m inlets on the AmeriFlux tower throughout the campaign indicated that O₃
600 was on average 5 ppb greater at the 27-m inlet, with the difference reaching as high as 34 ppb on 6 July and 20 July. The
601 probability distribution of vertical O₃ differences observed during Episode #3 is markedly different than those observed
602 during Episode #1, Episode #4, and the remainder of the campaign. This indicates that O₃ had a larger probability of being
603 between 0-10 ppb higher above the canopy during this episode compared to the rest of the campaign.

604 Based on Episode #1 and Episode #4, one of several potential driving factors of vertical differences for OA is a vertical
605 difference in particulate SO₄. Figure 7 indicates the vertical differences in OA and SO₄ relative to their respective above-
606 canopy concentrations. This metric is defined as “% PM Difference,” where PM is the given PM constituent and is equal to
607 the ΔPM constituent divided by the above-canopy PM concentration. Data that fall in the upper right and bottom left
608 quadrants correspond to higher above- and higher below-canopy concentrations, respectively. The vertical difference above
609 or below the canopy can be up to approximately 35% of the total available SO₄ or OA at the site. Figure 7 indicates that
610 there is a strong linear relationship between the %SO₄ Difference and %OA Difference during the campaign, even outside of
611 the Episodes defined here.

612 The concurrent features of vertical differences in OA factors and SO₄ observed in Episodes #1, #2, and #4 and OA
613 factors and O₃ in Episode #3 suggest that long-range regional transport (enhanced MO-OOA, SO₄, and/or O₃) is a key first
614 step in causing these differences. Local through-canopy mixing then determines whether the enhancement is above

615 (Episodes #1, #3, and #4) or below (Episode #2) the canopy. The transported material can then impact local chemistry.
616 Increased SO_4 likely increases aerosol hygroscopicity resulting in increased ALW, which could result in increased
617 partitioning of semi-volatile organics to the condensed phase (i.e., IEPOX-OA) (Budisulistiorini et al., 2017; El-Sayed et al.,
618 2018; Marais et al., 2016). Pre-existing OA (i.e., MO-OOA) transported with SO_4 aerosol could also play a role in the
619 partitioning of OA above the canopy during these episodes. Vertical gradients in O_3 coinciding with Episode #3 (higher O_3
620 above) could initiate relatively local formation of extremely low volatility compounds, which are first-generation oxidation
621 products of α -pinene and O_3 (Jokinen et al., 2015). Based on the WPSCF and backward trajectory clustering results, cooler,
622 northerly air masses associated with IEPOX-OA also could promote partitioning of semi-volatile organics to the particle
623 phase. It is important to note that it is difficult to conclude the exact chemical mechanisms that are influencing these events
624 due to their low mass loadings and episodic nature and the consistently higher above-canopy O_3 concentrations during the
625 campaign.
626



627
628 **Figure 7: Scatter plot of % difference in SO_4 (y-axis) and OA (x-axis) for the entire campaign. The % difference is**
629 **calculated as Δ Species / Above-Canopy Species concentration, and is representative of the normalized Δ Species**
630 **concentration.**
631

632 Understanding these events is important because uncoupled forest-canopy conditions have been observed in a number of
633 locations (Foken et al., 2012; Whitehead et al., 2010) and could indicate differences between above-canopy and surface level
634 PM. One-dimensional modeling has revealed that the timescales of turbulent transport inside a forest canopy can be much
635 shorter (minutes) than the timescale of aerosol dynamics and deposition (hours) (Rannik et al., 2016), but this evaluation
636 suggests that advective episodes can cause vertical gradients that are not locally driven. Above-canopy OA and particle
637 fluxes have been observed in other studies (Farmer et al., 2013; Pryor et al., 2007), suggesting the need for careful evaluation
638 of whether differences are driven by local chemistry, long-range transport, or a combination thereof.
639

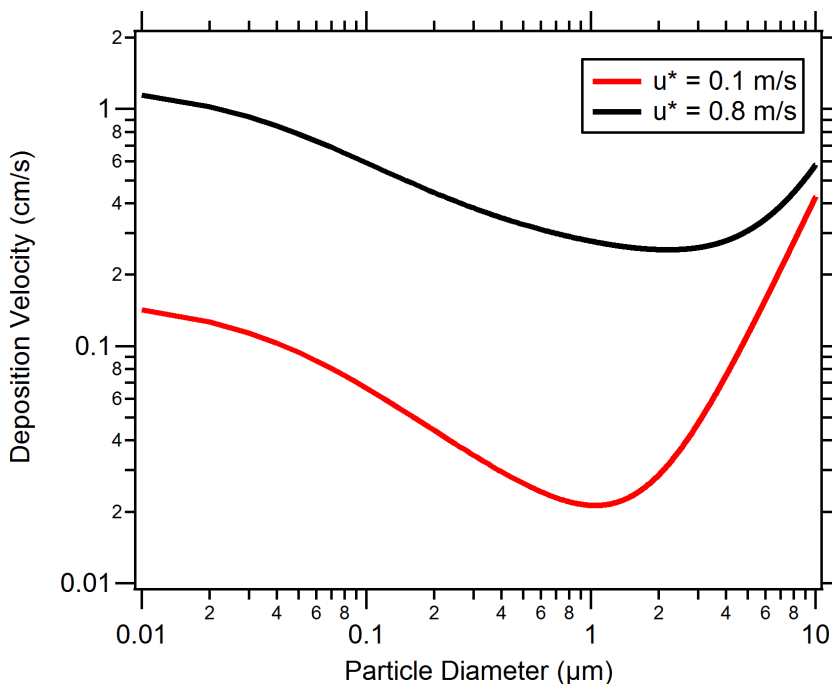
640 3.6 Particle dry deposition model

641 To investigate broadly the effects of canopy mixing on particle deposition in a forest canopy, a particle dry deposition
642 model is used. Note that we are not applying this through the canopy but to illustrate the relationship between deposition
643 and u^* . The resistance model for particle dry deposition assumes that the deposition process is controlled by three
644 resistances in series: aerodynamic, quasi-laminar, and canopy resistance (Seinfeld and Pandis, 2006). Details on the particle

645 dry deposition model are included in the SI. Conditions and parameters representative of the land use category, season, and
646 forest canopy present at the PROPHET site are used as model inputs.

647 Figure 8 displays model results for deposition velocity as a function of particle diameter under stable atmospheric
648 conditions. For illustration, test cases are shown for u^* values for low in-canopy mixing ($u^* = 0.1$ m/s) and high in-canopy
649 mixing ($u^* = 0.8$ m/s). Values of u^* were chosen based on the range of u^* values observed during the campaign at 29m on
650 the PROPHET tower. For the submicron particle diameter range (0.1 to 1 micron), a characteristic minimum in deposition
651 velocity is observed for both test cases at 1 micron diameter. Deposition modeling indicates that higher deposition velocities
652 are achieved in the high in-canopy mixing test case, implying that there is less canopy transport resistance to the surface and
653 more deposition in the canopy. This corresponds to Episode #2.

654



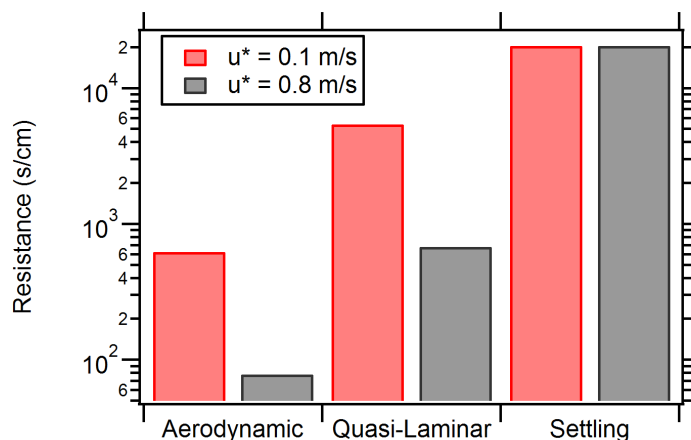
655

656 **Figure 8: Particle dry deposition velocity resistance model results plotted by particle diameter and friction velocity.**
657 **Two test cases of low and high friction velocity, representative of data collected at the PROPHET site, are plotted in**
658 **red and black solid lines, respectively. Land-use conditions and seasonal parameters similar to the PROPHET**
659 **campaign were used as inputs to the particle dry deposition model. Additional model parameters are provided in the**
660 **SI.**

661

662 Deposition modeling also indicates relatively lower deposition velocities for the low mixing condition test case, which
663 suggests that particles aloft are transported less efficiently into the forest (similar to the conditions present for Episodes #3
664 and #4). A comparison of the deposition resistances (shown in Figure 9) indicates that aerodynamic and quasi-laminar
665 resistances in the low-mixing test case are an order of magnitude greater than the high-mixing case. The settling removal
666 resistance is the same between both test cases because it is merely a function of diameter. A greater aerodynamic resistance
667 limits turbulent transport from the above-canopy layer to the surface layer and greater quasi-laminar layer resistance limits
668 transport to just above the surface by lowering particle impaction. In total, this result emphasizes the importance of in-
669 canopy transport and mixing in governing particle concentrations in forests.

670



671
 672 **Figure 8: Deposition and particle settling (accounts for the effect of sedimentation) resistances comparison for low**
 673 **and high friction velocities. Resistance comparison assumes a 1 micron particle diameter.**

674 4 Conclusions

675 In this study, source apportionment of OA using separate PMF analyses on inlets situated above and below a forest
 676 canopy resulted in three OA factors at a site in northern Michigan. Similarity in OA composition, concentration, and diurnal
 677 profiles was observed between the two inlets, suggesting that turbulent transport efficiently mixes OA across the canopy.
 678 However, OA factor vertical differences between the two inlets were observed during four separate episodes. During these
 679 episodes, vertical differences were both positive (greater concentrations above the canopy) and negative (greater
 680 concentrations below canopy). NR-PM₁ composition amongst these episodes was unique (Episode #1: MO-OOA dominant,
 681 Episode #2: SO₄ dominant, Episode #3: 91Fac dominant, Episode #4: IEPOX-OA dominant). Furthermore, the vertical
 682 difference concentrations can be 35% of the total available SO₄ or OA at the site. It has also been shown that relative
 683 vertical differences in SO₄ and OA are linearly associated, suggesting the role of regional SO₄ in vertical profiles of NR-PM₁
 684 in forested environments.

685 Using micrometeorological measurements, it has been shown in this work that periods of low in-canopy mixing
 686 conditions can be associated with the timing of vertical difference episodes where above-canopy concentrations are larger
 687 than those below. The opposite scenario is hypothesized to be associated with transport of air from aloft or with
 688 accumulation of material below canopy more rapidly than it is deposited. Either way, these results suggest that canopy
 689 mixing impacts particle levels. However, under low-mixing scenarios, it appears that enhancements as defined here depend
 690 on both these conditions and the presence of transported O₃ or SO₄ to enhance IEPOX-OA and 91Fac levels.

691 To the knowledge of the author, this is one of only a few studies that have assessed vertical profiles in OA factors
 692 above and below a forest canopy, and the first study to observe episodes of vertical differences in OA factors above and
 693 below a forest canopy. This work adds to the existing literature on aerosol chemistry in a forest canopy environment
 694 presented by Rizzo et al. (2010) and Whitehead et al. (2010) and to literature on vertical profiles of OA in an urban
 695 environment by Özturk et al. (2013).

696 To investigate the effects of forest canopies on SOA formation, small-scale models, such as those described in
 697 Schulze et al. (2017) and Ashworth et al. (2015), have been developed. The OA data from this work can be used to validate
 698 such models and are particularly relevant to these modeling efforts, as the models were developed using campaign data from
 699 the PROPHET site in 2009. Vertical transport and horizontal advection are both sources of uncertainty in current forest
 700 canopy-atmosphere exchange models, which are designed to focus on local processes. Ultimately, the vertical similarity in

701 NR-PM₁ OA composition observed in this study implies that it may be valid to assume that below-canopy OA composition
702 is generally representative of the OA composition in the atmospheric layer directly above the canopy and vice versa.
703 However, this work highlights that advection of regional pollution into forested regions can lead to in-canopy gradients that
704 are not present under purely local conditions.
705

706 **Data Availability**

707 Data are available through contacting the corresponding author.

708 **Author Contributions**

709 A.A.T.B. prepared the manuscript with input from all authors. A.A.T.B., H.W.W. and R.J.G. conceived of the study and
710 operated and analyzed the data from the HR-ToF-AMS. S.K. and A.L.S. investigated friction velocity and in-canopy
711 mixing. H.D.A. and D.B.M. collected and analyzed VOC data. J.H.F., M.H.E. and S.A. collected and analyzed trace gas
712 data and operated the MAQL.

713 **Competing Interests**

714 The authors declare they have no conflict of interest.

715 **Acknowledgements**

716 The assistance of all staff and collaborators at UMBS is gratefully acknowledged. We would like to thank Wei Wang at
717 University of Colorado Boulder for assistance in collecting O₃ data at the AmeriFlux tower and the Murphy group at the
718 University of Toronto for provision of nitrogen oxide data. This work was funded by the National Science Foundation
719 (NSF) under grant AGS-1552086. PTR-QiToF measurements during PROPHET-AMOS were also supported by NSF (grants
720 AGS-1428257+AGS-1148951). Trace gas and meteorological measurements on board the MAQL were also supported by
721 NSF (grant AGS-1552077).

722 **References**

- 723 Alwe, H.D., Millet, D.B., Chen, X., Raff, J.D., Payne, Z.C., Fledderman, K., 2019. Oxidation of Volatile Organic
724 Compounds as the Major Source of Formic Acid in a Mixed Forest Canopy. *Geophysical Research Letters* 0.
725 <https://doi.org/10.1029/2018GL081526>
- 726 Ashworth, K., Chung, S.H., Griffin, R.J., Chen, J., Forkel, R., Bryan, A.M., Steiner, A.L., 2015. FORest Canopy
727 Atmosphere Transfer (FORCAsT) 1.0: a 1-D model of biosphere–atmosphere chemical exchange. *Geoscientific*
728 *Model Development* 8, 3765–3784. <https://doi.org/10.5194/gmd-8-3765-2015>
- 729 Baldocchi, D., Guenther, A.B., Harley, P., Klinger, L., Zimmerman, P., Lamb, B., Westberg, H., 1995. The fluxes and air
730 chemistry of isoprene above a deciduous hardwood forest. *Philosophical Transactions: Physical Sciences and*
731 *Engineering* 351, 279–296.
- 732 Bergen, K.M., Dronova, I., 2007. Observing succession on aspen-dominated landscapes using a remote sensing-ecosystem
733 approach. *Landscape Ecology* 22, 1395–1410. <https://doi.org/10.1007/s10980-007-9119-1>
- 734 Berkowitz, C.M., Fast, J.D., Springston, S.R., Larsen, R.J., Spicer, C.W., Doskey, P.V., Hubbe, J.M., Plastridge, R., 1998.
735 Formation mechanisms and chemical characteristics of elevated photochemical layers over the northeast United
736 States. *J. Geophys. Res.* 103, 10631–10647. <https://doi.org/10.1029/97JD03751>

737 Bondy, A.L., Wang, B., Laskin, A., Craig, R.L., Nhliziyo, M.V., Bertman, S., Pratt, K.A., Shepson, P.B., Ault, A.P., 2017.
738 Inland Sea Spray Aerosol Transport and Incomplete Chloride Depletion: Varying Degrees of Reactive Processing
739 Observed during SOAS. *Environ. Sci. Technol.* <https://doi.org/10.1021/acs.est.7b02085>

740 Brown, S.S., Osthoff, H.D., Stark, H., Dubé, W.P., Ryerson, T.B., Warneke, C., de Gouw, J.A., Wollny, A.G., Parrish, D.D.,
741 Fehsenfeld, F.C., Ravishankara, A.R., 2005. Aircraft observations of daytime NO₃ and N₂O₅ and their implications
742 for tropospheric chemistry. *Journal of Photochemistry and Photobiology A: Chemistry* 176, 270–278.
743 <https://doi.org/10.1016/j.jphotochem.2005.10.004>

744 Bryan, A.M., Bertman, S.B., Carroll, M.A., Dusanter, S., Edwards, G.D., Forkel, R., Griffith, S., Guenther, A.B., Hansen,
745 R.F., Helmig, D., Jobson, B.T., Keutsch, F.N., Lefer, B.L., Pressley, S.N., Shepson, P.B., Stevens, P.S., Steiner,
746 A.L., 2012. In-canopy gas-phase chemistry during CABINEX 2009: sensitivity of a 1-D canopy model to vertical
747 mixing and isoprene chemistry. *Atmospheric Chemistry and Physics* 12, 8829–8849. <https://doi.org/10.5194/acp-12-8829-2012>

749 Budisulistiorini, S.H., Nenes, A., Carlton, A.G., Surratt, J.D., McNeill, V.F., Pye, H.O.T., 2017. Simulating Aqueous-Phase
750 Isoprene-Epoxydiol (IEPOX) Secondary Organic Aerosol Production During the 2013 Southern Oxidant and
751 Aerosol Study (SOAS). *Environmental Science & Technology* 51, 5026–5034.
752 <https://doi.org/10.1021/acs.est.6b05750>

753 Canagaratna, M.R., Jimenez, J.L., Kroll, J.H., Chen, Q., Kessler, S.H., Massoli, P., Hildebrandt Ruiz, L., Fortner, E.,
754 Williams, L.R., Wilson, K.R., Surratt, J.D., Donahue, N.M., Jayne, J.T., Worsnop, D.R., 2015. Elemental ratio
755 measurements of organic compounds using aerosol mass spectrometry: characterization, improved calibration, and
756 implications. *Atmospheric Chemistry and Physics* 15, 253–272. <https://doi.org/10.5194/acp-15-253-2015>

757 Carlton, A.G., Baker, K.R., 2011. Photochemical Modeling of the Ozark Isoprene Volcano: MEGAN, BEIS, and Their
758 Impacts on Air Quality Predictions. *Environmental Science & Technology* 45, 4438–4445.
759 <https://doi.org/10.1021/es200050x>

760 Carroll, M.A., Bertman, S.B., Shepson, P.B., 2001. Overview of the Program for Research on Oxidants: PHotochemistry,
761 Emissions, and Transport (PROPHET) summer 1998 measurements intensive. *Journal of Geophysical Research*
762 106.

763 Chang, Y., Deng, C., Cao, F., Cao, C., Zou, Z., Liu, S., Lee, X., Li, J., Zhang, G., Zhang, Y., 2017. Assessment of
764 carbonaceous aerosols in Shanghai, China – Part 1: long-term evolution, seasonal variations, and meteorological
765 effects. *Atmos. Chem. Phys.* 17, 9945–9964. <https://doi.org/10.5194/acp-17-9945-2017>

766 Cooper, O.R., Moody, J.L., Thornberry, T.D., Town, M.S., Carroll, M.A., 2001. PROPHET 1998 meteorological overview
767 and air-mass classification. *Journal of Geophysical Research* 106.

768 Cubison, M.J., Ortega, A.M., Hayes, P.L., Farmer, D.K., Day, D., Lechner, M.J., Brune, W.H., Apel, E., Diskin, G.S.,
769 Fisher, J.A., Fuelberg, H.E., Hecobian, A., Knapp, D.J., Mikoviny, T., Riemer, D., Sachse, G.W., Sessions, W.,
770 Weber, R.J., Weinheimer, A.J., Wisthaler, A., Jimenez, J.L., 2011. Effects of aging on organic aerosol from open
771 biomass burning smoke in aircraft and laboratory studies. *Atmospheric Chemistry and Physics* 11, 12049–12064.
772 <https://doi.org/10.5194/acp-11-12049-2011>

773 DeCarlo, P.F., Kimmel, J.R., Trimborn, A., Northway, M.J., Jayne, J.T., Aiken, A.C., Gonin, M., Fuhrer, K., Horvath, T.,
774 Docherty, K.S., others, 2006. Field-deployable, high-resolution, time-of-flight aerosol mass spectrometer.
775 *Analytical Chemistry* 78, 8281–8289.

776 Ditto, J.C., Barnes, E.B., Khare, P., Takeuchi, M., Joo, T., Bui, A.A.T., Lee-Taylor, J., Eris, G., Chen, Y., Aumont, B.,
777 Jimenez, J.L., Ng, N.L., Griffin, R.J., Gentner, D.R., 2018. An omnipresent diversity and variability in the chemical
778 composition of atmospheric functionalized organic aerosol. *Communications Chemistry* 1, 75.
779 <https://doi.org/10.1038/s42004-018-0074-3>

780 Draxler, R.R., Hess, G.D., 1998. An overview of the HYSPLIT_4 modeling system for trajectories, dispersion, and
781 deposition. *Australian meteorological magazine* 47.

782 El-Sayed, M.M.H., Ortiz-Montalvo, D.L., Hennigan, C.J., 2018. The effects of isoprene and NO_x on secondary organic
783 aerosols formed through reversible and irreversible uptake to aerosol water. *Atmospheric Chemistry and Physics*
784 18, 1171–1184. <https://doi.org/10.5194/acp-18-1171-2018>

785 Farmer, D.K., Chen, Q., Kimmel, J.R., Docherty, K.S., Nemitz, E., Artaxo, P.A., Cappa, C.D., Martin, S.T., Jimenez, J.L.,
786 2013. Chemically Resolved Particle Fluxes Over Tropical and Temperate Forests. *Aerosol Science and Technology*
787 47, 818–830. <https://doi.org/10.1080/02786826.2013.791022>

788 Fehsenfeld, F.C., Calvert, J.G., Fall, R., Goldan, P., Guenther, A., Hewitt, C.N., Lamb, B., Shaw, L., Trainer, M., Westberg,
789 H., Zimmerman, P., 1992. Emissions of volatile organic compounds from vegetation and the implications for
790 atmospheric chemistry. *Global Biogeochemical Cycles* 6.

791 Finnigan, J., 2000. Turbulence in plant canopies. *Annual Review of Fluid Mechanics* 32, 519–571.

792 Foken, T., Meixner, F.X., Falge, E., Zetzsch, C., Serafimovich, A., Bargsten, A., Behrendt, T., Biermann, T., Breuninger, C.,
793 Dix, S., Gerken, T., Hunner, M., Lehmann-Pape, L., Hens, K., Jocher, G., Kesselmeier, J., Lüers, J., Mayer, J.-C.,
794 Moravek, A., Plake, D., Riederer, M., Rütz, F., Scheibe, M., Siebicke, L., Sörgel, M., Staudt, K., Trebs, I.,
795 Tsokankunku, A., Welling, M., Wolff, V., Zhu, Z., 2012. Coupling processes and exchange of energy and reactive
796 and non-reactive trace gases at a forest site – results of the EGER experiment. *Atmospheric Chemistry and Physics*
797 12, 1923–1950. <https://doi.org/10.5194/acp-12-1923-2012>

798 Fuentes, J.D., Wang, D., Bowling, D.R., Potosnak, M., Monson, R.K., Goliff, W.S., Stockwell, W.R., 2007. Biogenic
799 Hydrocarbon Chemistry within and Above a Mixed Deciduous Forest. *Journal of Atmospheric Chemistry* 56, 165–
800 185. <https://doi.org/10.1007/s10874-006-9048-4>

801 Gao, W., Wesely, M.L., Doskey, P.V., 1993. Numerical modeling of the turbulent diffusion and chemistry of NO_x, O₃,
802 isoprene, and other reactive trace gases in and above a forest canopy. *Journal of Geophysical Research:*
803 *Atmospheres* 98, 18339–18353. <https://doi.org/10.1029/93JD01862>

804 Geron, C., Rasmussen, R., R. Arnsts, R., Guenther, A., 2000. A review and synthesis of monoterpene speciation from forests
805 in the United States. *Atmospheric Environment* 34, 1761–1781. [https://doi.org/10.1016/S1352-2310\(99\)00364-7](https://doi.org/10.1016/S1352-2310(99)00364-7)

806 Goldstein, A.H., Galbally, I.E., 2007. Known and unexplored organic constituents in the earth’s atmosphere. *Environmental*
807 *Science & Technology*.

808 Gordon, M., Staebler, R.M., Liggio, J., Vlasenko, A., Li, S.-M., Hayden, K., 2011. Aerosol flux measurements above a
809 mixed forest at Borden, Ontario. *Atmospheric Chemistry and Physics* 11, 6773–6786. <https://doi.org/10.5194/acp-11-6773-2011>

811 Guenther, A., Geron, C., Pierce, T., Lamb, B., Harley, P., Fall, R., 2000. Natural emissions of non-methane volatile organic
812 compounds, carbon monoxide, and oxides of nitrogen from North America. *Atmospheric Environment* 34, 2205–
813 2230.

814 Guenther, A., Hewitt, C.N., Erickson, D., Fall, R., Geron, C., Graedel, T., Harley, P., Klinger, L., Lerdau, M., McKay, W.A.,
815 Pierce, T., Scholes, B., Steinbrecher, R., Tallamraju, R., Taylor, J., Zimmerman, P., 1995. A global model of natural
816 volatile organic compound emissions. *Journal of Geophysical Research* 100.

817 Gunch, M.J., May, N.W., Wen, M., Bottenus, C.L.H., Gardner, D.J., VanReken, T.M., Bertman, S.B., Hopke, P.K., Ault,
818 A.P., Pratt, K.A., 2018. Ubiquitous influence of wildfire emissions and secondary organic aerosol on summertime
819 atmospheric aerosol in the forested Great Lakes region. *Atmospheric Chemistry and Physics* 18, 3701–3715.
820 <https://doi.org/10.5194/acp-18-3701-2018>

821 Holzinger, R., Lee, A., Paw, K.T., Goldstein, U.A.H., 2005. Observations of oxidation products above a forest imply
822 biogenic emissions of very reactive compounds. *Atmospheric Chemistry and Physics* 5, 67–75.

823 Hu, W.W., Campuzano-Jost, P., Palm, B.B., Day, D.A., Ortega, A.M., Hayes, P.L., Krechmer, J.E., Chen, Q., Kuwata, M.,
824 Liu, Y.J., de Sá, S.S., McKinney, K., Martin, S.T., Hu, M., Budisulistiorini, S.H., Riva, M., Surratt, J.D., St. Clair,
825 J.M., Isaacman-Van Wertz, G., Yee, L.D., Goldstein, A.H., Carbone, S., Brito, J., Artaxo, P., de Gouw, J.A., Koss,
826 A., Wisthaler, A., Mikoviny, T., Karl, T., Kaser, L., Jud, W., Hansel, A., Docherty, K.S., Alexander, M.L.,
827 Robinson, N.H., Coe, H., Allan, J.D., Canagaratna, M.R., Paulot, F., Jimenez, J.L., 2015. Characterization of a real-
828 time tracer for isoprene epoxydiols-derived secondary organic aerosol (IEPOX-SOA) from aerosol mass
829 spectrometer measurements. *Atmospheric Chemistry and Physics* 15, 11807–11833. <https://doi.org/10.5194/acp-15-11807-2015>

831 IPCC (Ed.), 2007. *Climate change 2007: the physical science basis: contribution of Working Group I to the Fourth*
832 *Assessment Report of the Intergovernmental Panel on Climate Change*. Cambridge University Press, Cambridge ;
833 New York.

834 Jimenez, J.L., Canagaratna, M.R., Donahue, N.M., Prevot, A.S.H., Zhang, Q., Kroll, J.H., DeCarlo, P.F., Allan, J.D., Coe,
835 H., Ng, N.L., Aiken, A.C., Docherty, K.S., Ulbrich, I.M., Grieshop, A.P., Robinson, A.L., Duplissy, J., Smith, J.D.,
836 Wilson, K.R., Lanz, V.A., Hueglin, C., Sun, Y.L., Tian, J., Laaksonen, A., Raatikainen, T., Rautiainen, J.,
837 Vaattovaara, P., Ehn, M., Kulmala, M., Tomlinson, J.M., Collins, D.R., Cubison, M.J., Dunlea, E., Huffman, J.A.,
838 Onasch, T.B., Alfarra, M.R., Williams, P.I., Bower, K., Kondo, Y., Schneider, J., Drewnick, F., Borrmann, S.,
839 Weimer, S., Demerjian, K., Salcedo, D., Cottrell, L., Griffin, R., Takami, A., Miyoshi, T., Hatakeyama, S.,
840 Shimono, A., Sun, J.Y., Zhang, Y.M., Dzepina, K., Kimmel, J.R., Sueper, D., Jayne, J.T., Herndon, S.C., Trimborn,
841 A.M., Williams, L.R., Wood, E.C., Middlebrook, A.M., Kolb, C.E., Baltensperger, U., Worsnop, D.R., 2009.
842 Evolution of Organic Aerosols in the Atmosphere. *Science* 326, 1525–1529.
843 <https://doi.org/10.1126/science.1180353>

844 Jokinen, T., Berndt, T., Makkonen, R., Kerminen, V.-M., Junninen, H., Paasonen, P., Stratmann, F., Herrmann, H.,
845 Guenther, A.B., Worsnop, D.R., Kulmala, M., Ehn, M., Sipilä, M., 2015. Production of extremely low volatile
846 organic compounds from biogenic emissions: Measured yields and atmospheric implications. *Proceedings of the*
847 *National Academy of Sciences* 112, 7123–7128. <https://doi.org/10.1073/pnas.1423977112>

848 Kanakidou, M., Seinfeld, J.H., Pandis, S.N., Barnes, I., Dentener, F.J., Facchini, M.C., Dingenen, R.V., Ervens, B., Nenes,
849 A., Nielsen, C.J., others, 2005. Organic aerosol and global climate modelling: a review. *Atmospheric Chemistry and*
850 *Physics* 5, 1053–1123.

851 Kroll, J.H., Donahue, N.M., Jimenez, J.L., Kessler, S.H., Canagaratna, M.R., Wilson, K.R., Altieri, K.E., Mazzoleni, L.R.,
852 Wozniak, A.S., Bluhm, H., Mysak, E.R., Smith, J.D., Kolb, C.E., Worsnop, D.R., 2011. Carbon oxidation state as a
853 metric for describing the chemistry of atmospheric organic aerosol. *Nature Chemistry* 3, 133–139.
854 <https://doi.org/10.1038/nchem.948>

855 Kruijt, B., Malhi, Y., Lloyd, J., Norbre, A.D., Miranda, A.C., Pereira, M.G.P., Culf, A., Grace, J., 2000. Turbulence
856 Statistics Above And Within Two Amazon Rain Forest Canopies. *Boundary-Layer Meteorology* 94, 297–331.
857 <https://doi.org/10.1023/A:1002401829007>

858 Leong, Y.J., Sanchez, N.P., Wallace, H.W., Cevik, B.K., Hernandez, C.S., Han, Y., Flynn, J.H., Massoli, P., Floerchinger,
859 C., Fortner, E.C., Herndon, S., Bean, J.K., Ruiz, L.H., Jeon, W., Choi, Y., Lefer, B., Griffin, R.J., 2017. Overview
860 of surface measurements and spatial characterization of submicrometer particulate matter during the DISCOVER-
861 AQ 2013 campaign in Houston, TX. *Journal of the Air & Waste Management Association* 67, 854–872.
862 <https://doi.org/10.1080/10962247.2017.1296502>

863 Makar, P.A., Staebler, R.M., Akingunola, A., Zhang, J., McLinden, C., Kharol, S.K., Pabla, B., Cheung, P., Zheng, Q., 2017.
864 The effects of forest canopy shading and turbulence on boundary layer ozone. *Nature Communications* 8, 15243,
865 <https://doi.org/10.1038/ncomms15243>

866 Marais, E.A., Jacob, D.J., Jimenez, J.L., Campuzano-Jost, P., Day, D.A., Hu, W., Krechmer, J., Zhu, L., Kim, P.S., Miller,
867 C.C., Fisher, J.A., Travis, K., Yu, K., Hanisco, T.F., Wolfe, G.M., Arkinson, H.L., Pye, H.O.T., Froyd, K.D., Liao,
868 J., McNeill, V.F., 2016. Aqueous-phase mechanism for secondary organic aerosol formation from isoprene:
869 application to the southeast United States and co-benefit of SO₂ emission controls. *Atmospheric Chemistry and*
870 *Physics* 16, 1603–1618. <https://doi.org/10.5194/acp-16-1603-2016>

871 Middlebrook, A.M., Bahreini, R., Jimenez, J.L., Canagaratna, M.R., 2012. Evaluation of Composition-Dependent Collection
872 Efficiencies for the Aerodyne Aerosol Mass Spectrometer using Field Data. *Aerosol Science and Technology* 46,
873 258–271. <https://doi.org/10.1080/02786826.2011.620041>

874 Millet, D.B., Alwe, H.D., Chen, X., Deventer, M.J., Griffis, T.J., Holzinger, R., Bertman, S.B., Rickly, P.S., Stevens, P.S.,
875 Léonardis, T., Locoge, N., Dusanter, S., Tyndall, G.S., Alvarez, S.L., Erickson, M.H., Flynn, J.H., 2018.
876 Bidirectional Ecosystem–Atmosphere Fluxes of Volatile Organic Compounds Across the Mass Spectrum: How
877 Many Matter? *ACS Earth and Space Chemistry* 2, 764–777. <https://doi.org/10.1021/acsearthspacechem.8b00061>

878 Miyazaki, Y., Fu, P., Ono, K., Tachibana, E., Kawamura, K., 2014. Seasonal cycles of water-soluble organic nitrogen
879 aerosols in a deciduous broadleaf forest in northern Japan. *J. Geophys. Res. Atmos.* 119, 1440–1454.
880 <https://doi.org/10.1002/2013JD020713>

881 Mohr, C., DeCarlo, P.F., Heringa, M.F., Chirico, R., Slowik, J.G., Richter, R., Reche, C., Alastuey, A., Querol, X., Seco, R.,
882 Peñuelas, J., Jiménez, J.L., Crippa, M., Zimmermann, R., Baltensperger, U., Prévôt, A.S.H., 2012. Identification

883 and quantification of organic aerosol from cooking and other sources in Barcelona using aerosol mass spectrometer
884 data. *Atmospheric Chemistry and Physics* 12, 1649–1665. <https://doi.org/10.5194/acp-12-1649-2012>

885 NADP, 2016. National Atmospheric Deposition Program, National Trends Network (NTN) Site Details [WWW Document].
886 URL <http://nadp.slh.wisc.edu/data/sites/siteDetails.aspx?net=NTN&id=MI09> (accessed 6.21.18).

887 Ng, N.L., Canagaratna, M.R., Zhang, Q., Jimenez, J.L., Tian, J., Ulbrich, I.M., Kroll, J.H., Docherty, K.S., Chhabra, P.S.,
888 Bahreini, R., Murphy, S.M., Seinfeld, J.H., Hildebrandt, L., Donahue, N.M., DeCarlo, P.F., Lanz, V.A., Prévôt,
889 A.S.H., Dinar, E., Rudich, Y., Worsnop, D.R., 2010. Organic aerosol components observed in Northern
890 Hemispheric datasets from Aerosol Mass Spectrometry. *Atmospheric Chemistry and Physics* 10, 4625–4641.
891 <https://doi.org/10.5194/acp-10-4625-2010>

892 Öztürk, F., Bahreini, R., Wagner, N.L., Dubé, W.P., Young, C.J., Brown, S.S., Brock, C.A., Ulbrich, I.M., Jimenez, J.L.,
893 Cooper, O.R., Middlebrook, A.M., 2013. Vertically resolved chemical characteristics and sources of submicron
894 aerosols measured on a Tall Tower in a suburban area near Denver, Colorado in winter. *J. Geophys. Res. Atmos.*
895 118, 2013JD019923. <https://doi.org/10.1002/2013JD019923>

896 Paatero, P., 1997. Least squares formulation of robust non-negative factor analysis. *Chemometrics and Intelligent Laboratory*
897 *Systems* 37, 23–35.

898 Paatero, P., Tapper, U., 1994. Positive matrix factorization: A non-negative factor model with optimal utilization of error
899 estimates of data values. *Environmetrics* 5, 111–126.

900 Polissar, A., 1999. The aerosol at Barrow, Alaska: long-term trends and source locations. *Atmospheric Environment* 33,
901 2441–2458. [https://doi.org/10.1016/S1352-2310\(98\)00423-3](https://doi.org/10.1016/S1352-2310(98)00423-3)

902 Polissar, A.V., Hopke, P.K., Harris, J.M., 2001. Source Regions for Atmospheric Aerosol Measured at Barrow, Alaska.
903 *Environ. Sci. Technol.* 35, 4214–4226. <https://doi.org/10.1021/es0107529>

904 Pryor, S.C., Larsen, S.E., Sørensen, L.L., Barthelmie, R.J., Grönholm, T., Kulmala, M., Launiainen, S., Rannik, Ü., Vesala,
905 T., 2007. Particle fluxes over forests: Analyses of flux methods and functional dependencies. *Journal of*
906 *Geophysical Research* 112. <https://doi.org/10.1029/2006JD008066>

907 Pugh, T. a. M., MacKenzie, A.R., Hewitt, C.N., Langford, B., Edwards, P.M., Furneaux, K.L., Heard, D.E., Hopkins, J.R.,
908 Jones, C.E., Karunaharan, A., Lee, J., Mills, G., Misztal, P., Moller, S., Monks, P.S., Whalley, L.K., 2010.
909 Simulating atmospheric composition over a South-East Asian tropical rainforest: performance of a chemistry box
910 model. *Atmospheric Chemistry and Physics* 10, 279–298. <https://doi.org/10.5194/acp-10-279-2010>

911 Rannik, Ü., Zhou, L., Zhou, P., Gierens, R., Mammarella, I., Sogachev, A., Boy, M., 2016. Aerosol dynamics within and
912 above forest in relation to turbulent transport and dry deposition. *Atmospheric Chemistry and Physics* 16, 3145–
913 3160. <https://doi.org/10.5194/acp-16-3145-2016>

914 Rizzo, L.V., Artaxo, P., Karl, T., Guenther, A.B., Greenberg, J., 2010. Aerosol properties, in-canopy gradients, turbulent
915 fluxes and VOC concentrations at a pristine forest site in Amazonia. *Atmospheric Environment* 44, 503–511.
916 <https://doi.org/10.1016/j.atmosenv.2009.11.002>

917 Schulze, B.C., Wallace, H.W., Bui, A.T., Flynn, J.H., Erickson, M.H., Alvarez, S., Dai, Q., Usenko, S., Sheesley, R.J.,
918 Griffin, R.J., 2018. The impacts of regional shipping emissions on the chemical characteristics of coastal submicron
919 aerosols near Houston, TX. *Atmospheric Chemistry and Physics* 18, 14217–14241. <https://doi.org/10.5194/acp-18-14217-2018>

920 Schulze, B.C., Wallace, H.W., Flynn, J.H., Lefer, B.L., Erickson, M.H., Jobson, B.T., Dusanter, S., Griffith, S.M., Hansen,
921 R.F., Stevens, P.S., VanReken, T., Griffin, R.J., 2017. Differences in BVOC oxidation and SOA formation above
922 and below the forest canopy. *Atmospheric Chemistry and Physics* 17, 1805–1828. <https://doi.org/10.5194/acp-17-1805-2017>

923 Seinfeld, J.H., Pandis, S.N., 2006. *Atmospheric chemistry and physics : from air pollution to climate change*. Hoboken, N.J. :
924 John Wiley, ©2006.

925 Sheesley, R.J., Schauer, J.J., Bean, E., Kenski, D., 2004. Trends in Secondary Organic Aerosol at a Remote Site in
926 Michigan's Upper Peninsula. *Environmental Science & Technology* 38, 6491–6500.
927 <https://doi.org/10.1021/es049104q>

928 Sirois, A., Bottenheim, J.W., 1995. Use of backward trajectories to interpret the 5-year record of PAN and O₃ ambient air
929 concentrations at Kejimikujik National Park, Nova Scotia. *Journal of Geophysical Research* 100, 2867.
930 <https://doi.org/10.1029/94JD02951>

- 933 Stein, A.F., Draxler, R.R., Rolph, G.D., Stunder, B.J.B., Cohen, M.D., Ngan, F., 2015. NOAA's HYSPLIT Atmospheric
934 Transport and Dispersion Modeling System. *Bulletin of the American Meteorological Society* 96, 2059–2077.
935 <https://doi.org/10.1175/BAMS-D-14-00110.1>
- 936 Steiner, A.L., Pressley, S.N., Botros, A., Jones, E., Chung, S.H., Edburg, S.L., 2011. Analysis of coherent structures and
937 atmosphere-canopy coupling strength during the CABINEX field campaign. *Atmospheric Chemistry and Physics*
938 11, 11921–11936. <https://doi.org/10.5194/acp-11-11921-2011>
- 939 Stroud, C., Makar, P., Karl, T., Guenther, A., Geron, C., Turnipseed, A., Nemitz, E., Baker, B., Potosnak, M., Fuentes, J.D.,
940 2005. Role of canopy-scale photochemistry in modifying biogenic-atmosphere exchange of reactive terpene
941 species: Results from the CELTIC field study. *Journal of Geophysical Research: Atmospheres* 110.
942 <https://doi.org/10.1029/2005JD005775>
- 943 Thomas, C., Foken, T., 2007. Flux contribution of coherent structures and its implications for the exchange of energy and
944 matter in a tall spruce canopy. *Boundary-Layer Meteorology* 123, 317–337. <https://doi.org/10.1007/s10546-006-9144-7>
- 945
- 946 Thornberry, T., Carroll, M.A., Keeler, G.A., Sanford, S., Bertman, S.B., Pippin, M.R., Ostling, K., Grossenbacher, J.W.,
947 Shepson, P.B., Cooper, O.R., Moody, J.L., Stockwell, W.R., 2001. Observations of reactive oxidized nitrogen and
948 speciation of NO_y during the PROPHET summer 1998 intensive. *Journal of Geophysical Research* 106, 359–386.
- 949 Toma, S., Bertman, S., 2012. The atmospheric potential of biogenic volatile organic compounds from needles of white pine
950 (*Pinus strobus*) in Northern Michigan. *Atmospheric Chemistry and Physics* 12, 2245–2252.
951 <https://doi.org/10.5194/acp-12-2245-2012>
- 952 Ulbrich, I.M., Canagaratna, M.R., Zhang, Q., Worsnop, D.R., Jimenez, J.L., 2009. Interpretation of organic components
953 from Positive Matrix Factorization of aerosol mass spectrometric data. *Atmospheric Chemistry and Physics* 9,
954 2891–2918.
- 955 US Census Bureau, 2018. City and Town Population Totals: 2010-2016 [WWW Document]. URL
956 <https://www.census.gov/data/tables/2016/demo/popest/total-cities-and-towns.html> (accessed 1.24.18).
- 957 VanReken, T.M., Mwaniki, G.R., Wallace, H.W., Pressley, S.N., Erickson, M.H., Jobson, B.T., Lamb, B.K., 2015. Influence
958 of air mass origin on aerosol properties at a remote Michigan forest site. *Atmospheric Environment* 107, 35–43.
959 <https://doi.org/10.1016/j.atmosenv.2015.02.027>
- 960 Wallace, H.W., Sanchez, N.P., Flynn, J.H., Erickson, M.H., Lefer, B.L., Griffin, R.J., 2018. Source apportionment of
961 particulate matter and trace gases near a major refinery near the Houston Ship Channel. *Atmospheric Environment*
962 173, 16–29. <https://doi.org/10.1016/j.atmosenv.2017.10.049>
- 963 Wang, Y.Q., 2014. MeteInfo: GIS software for meteorological data visualization and analysis: Meteorological GIS
964 software. *Meteorological Applications* 21, 360–368. <https://doi.org/10.1002/met.1345>
- 965 Wang, Y.Q., Zhang, X.Y., Draxler, R.R., 2009. TrajStat: GIS-based software that uses various trajectory statistical analysis
966 methods to identify potential sources from long-term air pollution measurement data. *Environmental Modelling &*
967 *Software* 24, 938–939. <https://doi.org/10.1016/j.envsoft.2009.01.004>
- 968 Whitehead, J.D., Gallagher, M.W., Dorsey, J.R., Robinson, N., Gabey, A.M., Coe, H., McFiggans, G., Flynn, M.J., Ryder,
969 J., Nemitz, E., Davies, F., 2010. Aerosol fluxes and dynamics within and above a tropical rainforest in South-East
970 Asia. *Atmospheric Chemistry and Physics* 10, 9369–9382. <https://doi.org/10.5194/acp-10-9369-2010>
- 971 Wiedinmyer, C., Greenberg, J., Guenther, A., Hopkins, B., Baker, K., Geron, C., Palmer, P.I., Long, B.P., Turner, J.R.,
972 Pétron, G., Harley, P., Pierce, T.E., Lamb, B., Westberg, H., Baugh, W., Koerber, M., Janssen, M., 2005. Ozarks
973 Isoprene Experiment (OZIE): Measurements and modeling of the “isoprene volcano.” *Journal of Geophysical*
974 *Research: Atmospheres* 110. <https://doi.org/10.1029/2005JD005800>
- 975 Wolfe, G.M., Thornton, J.A., 2011. The Chemistry of Atmosphere-Forest Exchange (CAFE) Model – Part 1: Model
976 description and characterization. *Atmospheric Chemistry and Physics* 11, 77–101. <https://doi.org/10.5194/acp-11-77-2011>
- 977
- 978 Xu, L., Pye, H.O.T., He, J., Chen, Y.L., Murphy, B.N., Ng, N.L., 2018. Experimental and model estimates of the
979 contributions from biogenic monoterpenes and sesquiterpenes to secondary organic aerosol in the southeastern
980 United States. *Atmospheric Chemistry and Physics* 18, 12613–12637. <https://doi.org/10.5194/acp-18-12613-2018>
- 981 Xu, L., Suresh, S., Guo, H., Weber, R.J., Ng, N.L., 2015. Aerosol characterization over the southeastern United States using
982 high-resolution aerosol mass spectrometry: spatial and seasonal variation of aerosol composition and sources with a

983 focus on organic nitrates. *Atmospheric Chemistry and Physics* 15, 7307–7336. <https://doi.org/10.5194/acp-15-7307->
984 2015

985 Zhang, Q., Jimenez, J.L., Canagaratna, M.R., Allan, J.D., Coe, H., Ulbrich, I., Alfarra, M.R., Takami, A., Middlebrook,
986 A.M., Sun, Y.L., Dzepina, K., Dunlea, E., Docherty, K., DeCarlo, P.F., Salcedo, D., Onasch, T., Jayne, J.T.,
987 Miyoshi, T., Shimojo, A., Hatakeyama, S., Takegawa, N., Kondo, Y., Schneider, J., Drewnick, F., Borrmann, S.,
988 Weimer, S., Demerjian, K., Williams, P., Bower, K., Bahreini, R., Cottrell, L., Griffin, R.J., Rautiainen, J., Sun,
989 J.Y., Zhang, Y.M., Worsnop, D.R., 2007. Ubiquity and dominance of oxygenated species in organic aerosols in
990 anthropogenically-influenced Northern Hemisphere midlatitudes: Ubiquity and dominance of oxygenated OA.
991 *Geophysical Research Letters* 34, 6. <https://doi.org/10.1029/2007GL029979>

992 Zhang, Q., Jimenez, J.L., Canagaratna, M.R., Ulbrich, I.M., Ng, N.L., Worsnop, D.R., Sun, Y., 2011. Understanding
993 atmospheric organic aerosols via factor analysis of aerosol mass spectrometry: a review. *Analytical and*
994 *Bioanalytical Chemistry* 401, 3045–3067. <https://doi.org/10.1007/s00216-011-5355-y>

995 Zhang, Q., Worsnop, D.R., Canagaratna, M.R., Jimenez, J.L., 2005. Hydrocarbon-like and oxygenated organic aerosols in
996 Pittsburgh: insights into sources and processes of organic aerosols. *Atmospheric Chemistry and Physics* 5, 3289–
997 3311.